JℱM PAPERS

Predicting burst events in a forced two-dimensional flow: a wavelet-based analysis

Anagha Madhusudanan[1,2,†] and Rich R. Kerswell[3]

[1]Isaac Newton Institute for Mathematical Sciences, 20 Clarkson Road, Cambridge CB3 0EH, UK

[2]Department of Aerospace Engineering, Indian Institute of Science, Mathikere, Bengaluru, Karnataka 560012, India

[3]Department of Applied Mathematics and Theoretical Physics, Centre for Mathematical Sciences, Wilberforce Road, Cambridge CB3 0WA, UK

Predicting and perhaps mitigating against rare, extreme events in fluid flows is an important challenge. Due to the time-localised nature of these events, Fourier-based methods prove inefficient in capturing them. Instead, this paper uses wavelet-based methods to understand the underlying patterns in a forced flow over a 2-torus which has intermittent high-energy burst events interrupting an ambient low-energy 'quiet' flow. Two wavelet-based methods are examined to predict burst events: (i) a wavelet proper orthogonal decomposition (WPOD) based method which uncovers and utilises the key flow patterns seen in the quiet regions and the bursting episodes; and (ii) a wavelet resolvent analysis (WRA) based method that relies on the forcing structures which amplify the underlying flow patterns. These methods are compared with a straightforward energy tracking approach which acts as a benchmark. Both the wavelet-based approaches succeed in producing better predictions than a simple energy criterion, i.e. earlier prediction times and/or fewer false positives and the WRA-based technique always performs better than WPOD. However, the improvement of WRA over WPOD is not as substantial as anticipated. We conjecture that this is because the mechanism for the bursts in the flow studied is found to be largely modal, associated with the unstable eigenfunction of the Navier–Stokes operator linearised around the mean flow. The WRA approach should deliver much better improvement over the WPOD approach for generically non-modal bursting mechanisms where there is a lag between the imposed forcing and the final response pattern.

Key words: Navier–Stokes equations, low-dimensional models, intermittency

† Email address for correspondence: anaghamadhu91@gmail.com

1003 A5-1

1. Introduction

Intermittent extreme events, characterised by a sudden increase in observables like energy or dissipation, are frequently encountered in both natural and engineering fluid flow systems. Some examples include extreme weather events (e.g. Neelin *et al.* 1998), rogue waves in the ocean (e.g. Dysthe, Krogstad & Müller 2008) and high dissipation events in turbulent flows (e.g. Chandler & Kerswell 2013; Yeung, Zhai & Sreenivasan 2015). These events can have significant impacts. Understanding the mechanisms that generate such events, and predicting them, are therefore active areas of research (Farazmand & Sapsis 2019*b*; Sapsis 2021). For instance, Donzis & Sreenivasan (2010) analysed direct numerical simulation (DNS) data to identify the observables that act as precursors to the intermittent events. In another work, Babaee & Sapsis (2016) used data to identify time-dependent orthonormal bases that characterise the transient instabilities in a system, which were then used to forecast extreme events (Farazmand & Sapsis 2016). However, working with time-dependent modes can become computationally expensive, and therefore a variational framework that identified static structures responsible for the extreme events was formulated by Farazmand & Sapsis (2017, 2019*b*). By tracking these identified structures, methods to predict and control the burst events were introduced (Blonigan, Farazmand & Sapsis 2019; Farazmand & Sapsis 2019*a*). A graph theoretic approach that uses clustering algorithms to find a hierarchy of coherent structures in intermittent flows has also been used (Schmid, García-Gutierrez & Jiménez 2018). More recently, the use of machine learning to identify and control extreme events has also gained popularity (e.g. Wan *et al.* 2018; Guth & Sapsis 2019; Pyragas & Pyragas 2020; Qi & Majda 2020; Doan, Polifke & Magri 2021; Racca & Magri 2022; Rudy & Sapsis 2022; Fox, Constante-Amores & Graham 2023). Another method, and one that is of more direct relevance to the current work, is the use of a variation of proper orthogonal decomposition (POD), called conditional-POD, to identify the dominant structures that are responsible for intermittent events (Schmidt & Schmid 2019).

Due to the time-localised nature of intermittent events, the Fourier basis is generally inefficient at characterising them. Wavelets are better adapted for this purpose, which suggests that wavelet-based methods could potentially provide another class of techniques for understanding and predicting intermittent events. Wavelets have found application in the analysis of turbulent signals since the early 1990s (e.g. Farge & Rabreau 1988; Meneveau 1991; Farge 1992). Since then, they have found varied applications in turbulence such as, for instance, extraction of the coherent and incoherent parts of a turbulent flow field (e.g. Farge, Pellegrino & Schneider 2001; Farge *et al.* 2003; Farge, Schneider & Devynck 2006) and development of simulation methods using wavelet-based numerical algorithms and turbulence models (see review by Schneider & Vasilyev 2010). Wavelet coefficients have also been used for detecting pipe bursts in water distribution systems (Srirangarajan *et al.* 2013) and predicting rogue waves (Bayındır 2016). Data-driven decomposition techniques based on wavelets have been introduced by Floryan & Graham (2021) to generate a hierarchical orthogonal basis for a flow and by Ren, Mao & Fu (2021) to extract the different dominant scales in a flow. Recent studies by Gupta *et al.* (2022), Krah *et al.* (2022) and Barthel & Sapsis (2023) have used wavelet analysis along with POD for identifying coherent structures in intermittent flows. In a parallel line of work, Ballouz, Dawson & Bae (2023*a*) and Ballouz *et al.* (2023*b*) extended the extensively used resolvent analysis technique to incorporate a temporal wavelet basis, thereby broadening the scope of the analysis.

In the current work, we aim to contribute towards understanding and predicting intermittent high-energy events in fluid flows by employing wavelet-based methods.

A two-dimensional (2-D) Kolmogorov flow at a Reynolds number of 40, forced by a sinusoidal body force with wavenumber 4, is considered. This flow is temporally characterised by a persistent quiet region that is intermittently interrupted by high-energy burst events (e.g. Chandler & Kerswell 2013; Page, Brenner & Kerswell 2021). To understand the temporal characteristics of the flow, we first project it onto a wavelet basis. Two wavelet-based methods will then be used to analyse the flow: (i) wavelet-based proper orthogonal decomposition (WPOD) to distinguish the dominant flow patterns of the quiet region and burst events and (ii) wavelet-based resolvent analysis (WRA) to identify forcing structures that generate the quiet region and burst events. The identification of these flow patterns poses a question: Can these patterns be utilised to predict oncoming burst events? We will therefore explore whether tracking the flow patterns obtained from WPOD (wavelet-based prediction method 1) and from WRA (wavelet-based prediction method 2) enables prediction of oncoming burst events. The predictions will be compared with those obtained from the more straightforward approach of tracking the energy of the flow.

We find that both the WPOD-based and the WRA-based methods give better predictions when compared with the energy-based method, i.e. earlier prediction times and/or fewer false positives. Additionally, the WRA-based method outperforms the WPOD-based method. This improvement, however, is not as significant as initially expected. Energy amplification in the flow considered here is likely caused by normal-mode mechanisms, where the amplification arises due to the system being excited at a frequency close to its eigenvalue (Trefethen *et al.* 1993). This could potentially explain the prediction performance observed here (see § 6). There is therefore a future need to assess how the prediction performance changes for flows governed by non-normal energy amplification mechanisms, where we can expect a lag between the forcing and the final response pattern.

The outline of the rest of this manuscript is as follows. We first introduce the 2-D Kolmogorov flow in § 2. The aim thereafter is to decompose the flow into the quiet region and the burst events. The efficiency of the wavelet basis in achieving such a decomposition is shown in § 3.4, and this is compared with the efficiency of the Fourier basis in § 3.1. Thereafter, in § 4, we probe the underlying flow patterns in this intermittent flow using WPOD. Predictions of the burst events obtained by tracking these WPOD modes (WPOD-based prediction method) are then studied in § 4.5. These predictions are compared with those obtained from a straightforward energy-tracking approach. Following this, in § 5 we use WRA to distinguish the structures that force the quiet region and burst events. Predictions obtained from tracking these forcing structures (WRA-based prediction method) are then compared with those obtained from the WPOD-based and energy-based methods in § 5.5. Following this, in § 6 we will look at a more detailed comparison of the performances of the prediction methods and also implications for future work. A final discussion follows in § 7.

2. Two-dimensional Kolmogorov flow

In this section, we consider the 2-D Kolmogorov flow. We will first discuss the linearised Navier–Stokes equations that describe the flow (§ 2.1), and thereafter consider the data obtained from the DNS of this flow (§§ 2.2 and 2.3).

2.1. *Linearised Navier–Stokes equations*

The intermittent flow that we use as our example in this work is the incompressible 2-D Kolmogorov flow. The two dimensions are denoted by x and y, respectively. The domain

is doubly periodic, with size L_x in the x-direction and L_y in the y-direction. The flow is forced in the x-direction by a sinusoidal body forcing of the form $\zeta \sin(2\pi n\grave{y}/L_y)$, where ζ is the amplitude of the forcing per unit mass of fluid, n is the wavenumber of the forcing and $\grave{y}$ indicates the dimensional y-coordinate. The mean velocity is $U(y)\hat{i}$, where $(\hat{i}, \hat{j})$ are unit vectors in the (x, y) directions. The mean is here defined over the x-direction and time. Additionally, it is symmetrised in the y-direction (why such a symmetrisation is required is discussed in § 2.3). The fluctuations of velocities around this mean are denoted by u and v in the x and y directions, respectively. Pressure is denoted by p and time by t. The length scale $L_y/2\pi$ and time scale $\sqrt{L_y/2\pi\zeta}$ are used to non-dimensionalise the system. The non-dimensional number that characterises this system is the Reynolds number, defined as $Re := (\sqrt{\zeta}/\nu)(L_y/2\pi)^{(3/2)}$, where ν is the kinematic viscosity. Here, we consider a flow with $n = 4$, $Re = 40$ and $L_x = L_y = 2\pi$, which is a regime characterised by intermittent burst events as will be discussed in § 2.2.

The non-dimensional equations linearised around the mean state $(U(y), 0)$ are

$$\frac{\partial \boldsymbol{u}}{\partial t} + U\frac{\partial \boldsymbol{u}}{\partial x} + v\frac{\partial U}{\partial y}\hat{i} + \boldsymbol{\nabla} p - \frac{1}{Re}\nabla^2 \boldsymbol{u} = \underbrace{\overline{\boldsymbol{u} \cdot \boldsymbol{\nabla u}} - \boldsymbol{u} \cdot \boldsymbol{\nabla u}}_{\boldsymbol{f}}, \quad \boldsymbol{\nabla} \cdot \boldsymbol{u} = 0, \qquad (2.1a,b)$$

where $\boldsymbol{u} = (u, v)$. The nonlinear terms of the equation $\overline{\boldsymbol{u} \cdot \boldsymbol{\nabla u}} - \boldsymbol{u} \cdot \boldsymbol{\nabla u}$ are hereafter represented by a forcing term $\boldsymbol{f} = (f_x, f_y)$, where f_x and f_y represent the forcing to the x and y momentum equations, respectively.

Using the incompressibility condition and taking the curl of (2.1*a*), we obtain the vorticity (ω) form of the equation as

$$\frac{\partial \omega}{\partial t} + \left[U\frac{\partial}{\partial x} - \frac{1}{Re}\Delta - U''\Delta^{-1}\frac{\partial}{\partial x} \right]\omega = F, \qquad (2.2)$$

where $\omega := \partial v/\partial x - \partial u/\partial y$ and $F := \partial f_y/\partial x - \partial f_x/\partial y$. Let us consider a Fourier transform in the homogeneous x-direction. The one-dimensional (1-D) discrete Fourier transform of ω gives

$$\omega(x, y, t) = \sum_{k_x = -(N_x/2)}^{(N_x/2)} \tilde{\omega}(y, t; k_x)\exp(ik_x x), \qquad (2.3)$$

where $\tilde{\ }$ represents the 1-D Fourier transform, k_x is the streamwise wavenumber non-dimensionalised by $L_y/2\pi$ and N_x is the number of grid points used to discretise the x-direction. Similarly, if $\tilde{F}$ is the 1-D Fourier transform of F, we obtain the following equation:

$$\dot{\tilde{\omega}}(y, t; k_x) + \boldsymbol{A}\tilde{\omega}(y, t; k_x) = \tilde{F}(y, t; k_x), \qquad (2.4)$$

where $\dot{(\ )}$ denotes the derivative in time. The matrix $\boldsymbol{A}$ contains the finite-dimensional discrete approximations of the linearised momentum equation from (2.2) in terms of the 1-D Fourier transforms with $\partial/\partial x$ replaced by ik_x.

2.2. *Direct numerical simulation data*

To obtain the DNS data for the 2-D Kolmogorov flow, we used the pseudo-spectral code as used in Chandler & Kerswell (2013). We consider the flow at a Reynolds number $Re = 40$ and forcing frequency $n = 4$. The DNS was run on a grid with $N_x = 256$ points in
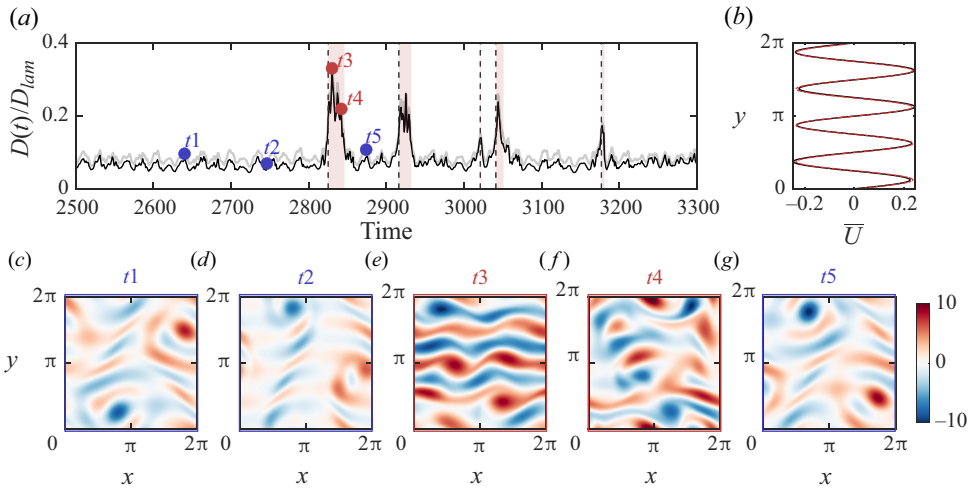
Figure 1. (*a*) The time series of $D(t)/D_{lam}$ from the full data is shown in grey for a sample time interval. Additionally, the time series obtained from just the streamwise wavenumbers of $|k_x| \leq 3$ is shown in black. Burst events, defined as times when $D(t)/D_{lam} > 0.15$, are shown as the red-shaded regions, with dashed black vertical lines indicating the beginnings of the burst events. (*c–g*) The vorticity field at the five time instances $t1–t5$ indicated in (*a*) are also shown, where the contours indicate positive (red) and negative (blue) vorticity, respectively. The colour limits are kept the same across the five time snapshots. In (*b*) the mean profile obtained from the data (black line) is compared with the symmetrised mean profile (red line).

the x-direction and $N_y = 257$ points in the y-direction. Figure 1(*a*) shows the time series of total dissipation $D(t) := \langle \omega, \omega \rangle_{x,y}$ normalised by the laminar dissipation rate $D_{lam} := Re/(2n^2)$. Here, $\langle a, b \rangle_{x,y}$ denotes the inner product $\int_0^{L_x} \int_0^{L_y} b^*(x, y, t) a(x, y, t) \, dx \, dy$. The time series represented by the grey line is obtained from the full dataset. On the other hand, the time series in black is obtained by retaining only the smallest streamwise wavenumbers with $|k_x| \leq 3$. The black line follows the grey line reasonably well, thereby suggesting that the $|k_x| \leq 3$ modes are responsible for the dominant dynamics in the flow. Example snapshots of the flow at the five times denoted in figure 1(*a*) are shown in figure 1(*c–g*), where the red and blue contours represent the positive and negative vorticity fluctuations, respectively. Here again, we observe the presence of large-scale structures in the flow, further confirming that the smallest wavenumbers dominate the flow dynamics. This is consistent with the observations in Page *et al.* (2021). For the rest of this manuscript, we therefore project the full DNS data onto the $|k_x| \leq 3$ modes, and use the truncated data for the POD and resolvent-based analyses. This truncation using a Fourier transform is not essential for the work that follows, but just allows us to expedite the computations.

Considering the burst events, if we define them as times when $D(t)/D_{lam} \geq 0.15$ (Page *et al.* 2021), then they are indicated by the red-shaded regions in figure 1(*a*) (the vertical black dashed lines therefore indicate the beginnings of these burst events). Throughout the manuscript, we use this criterion of $D(t)/D_{lam} \geq 0.15$ to define burst events, and also $D(t)/D_{lam} \leq 0.1$ to identify regions that are assured to be quiet. Changing these numbers for $D(t)/D_{lam}$ will impact the quantitative values obtained. However, we are here interested only in the relative differences between the prediction methods, and we can expect these trends to remain insensitive to this change. Appendix C confirms that these relative trends are not impacted by this definition of the burst event.

1003 A5-5

2.3. *Symmetrisation of the mean profile*

Let us briefly consider the mean velocity profiles $U(y)$ obtained from this flow, where the mean is defined over the x-direction and time. The converged mean profile is expected to follow two symmetries: (i) a shift-and-reflect symmetry $\mathcal{S} : U(y) \rightarrow -U(y + \pi/4)$ and (ii) a rotational symmetry $\mathcal{R} : U(y) \rightarrow -U(-y)$. Chandler & Kerswell (2013) investigated the mean profiles obtained from 10^5 time units of the flow, and observed that even this was not long enough to obtain a converged mean profile that shows the expected symmetries. The black line (which is asymmetric when investigated closely) in figure 1(*b*) represents the mean computed from 16 800 snapshots of data. This obtained mean does not follow the symmetries. Therefore, as done in Chandler & Kerswell (2013), here, we use a symmetrised mean profile $U(y)$ which is extracted from the asymmetric mean obtained from the DNS $U_a(y)$ as

$$U(y) := \frac{1}{2n} \sum_{m=0}^{2n-1} \mathcal{S}^{-m} U^{\dagger}(\mathcal{S}^m y), \quad \text{where } U^{\dagger} := \frac{1}{2}[U_a(y) + \mathcal{R}^{-1} U_a(\mathcal{R}y)]. \tag{2.5}$$

Here, $n = 4$. The definitions of the symmetry operations follows from before as $\mathcal{R}^{-1} : U(y) \rightarrow -U(-y)$, $\mathcal{S}^m : U(y) \rightarrow (-1)^m U(y + m\pi/4)$ and $\mathcal{S}^{-m} : U(y) \rightarrow (-1)^m U(y - m\pi/4)$, where $0 \leq m \leq (2n - 1)$. The red line in figure 1(*b*) shows $U(y)$, and this symmetrised mean will be used for the rest of this work.

3. Decomposing the flow into quiet regions and burst events

Both the WPOD-based and WRA-based prediction methods that will be introduced later depend on the identification of flow structures that exist in the quiet region and the burst events. To identify such structures, it is necessary to first decompose the flow into the quiet region and the burst events.

3.1. *Decomposing the flow: Fourier bases*

In this section, we use the Fourier basis for decomposing the flow into the quiet region and the burst events. Looking ahead, isolating the time-localised burst events using the global Fourier basis may prove to be inefficient. Therefore, the aim of this section is to provide motivation for moving towards using a wavelet basis.

We are interested in analysing a burst event, and require multiple realisations of such events. Consider N_e realisations of the burst event, each containing N_t time snapshots of vorticity $\omega(x, y, t)$ spaced apart by time dt. Each of the N_e realisations is therefore $T = N_t dt$ long. Here, to obtain one such realisation of the burst event, the start of a burst event T_b is first identified using the condition $D(t)/D_{lam} \geq 0.15$. The realisation of the burst event is then taken to be $T_b - 100 \leq t \leq T_b + 100$. (The reasons for choosing such time-windows, instead of the more generally used consecutive time blocks, will become apparent when considering the energy of the wavelet coefficients in figure 4 of the next section.) For the DNS dataset considered here, we split the data to obtain $N_e = 50$ realisations of the burst event, with each realisation having $N_t = 200$ and $dt = 1$, and therefore $T = 200$. It is ensured that no two realisations of the burst event have more than 50 % overlap.
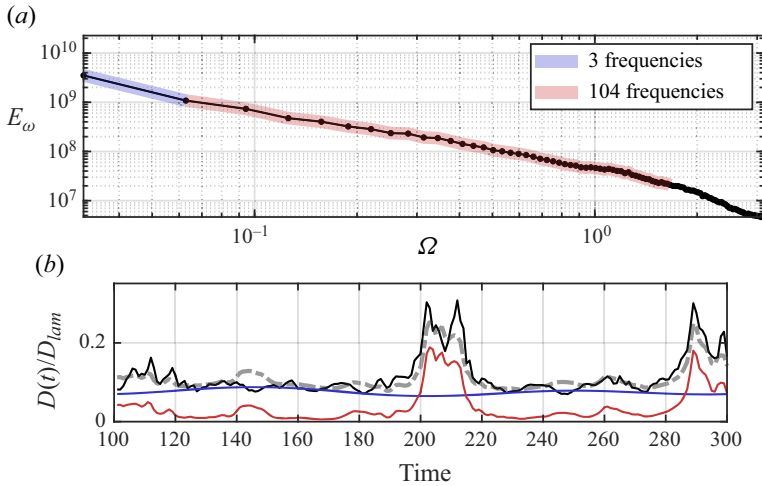
Figure 2. (*a*) The ensemble-averaged Fourier spectrum is shown in black, and the frequencies used to reconstruct the quiet region and the burst event, separately, are shaded in blue and red, respectively. (*b*) The full data (for $k_x = 0, 1, 2, 3$) (black) are compared with the reconstructions of the quiet region (blue) and the burst event (red) using the shaded frequencies in (*a*). For comparison, the grey dashed-dot line shows the sum of the blue and the red lines.

Let us now consider the Fourier transform of the vorticity $\omega(x, y, t)$ in time

$$\omega(x, y, t) = \sum_{\Omega=0}^{N_t-1} \breve{\omega}(x, y; \Omega) \exp(i(2\pi/T)\Omega t), \tag{3.1}$$

where $(\breve{\cdot})$ here represents the temporal Fourier transform. The corresponding Fourier spectrum is $E_\omega(\Omega) = [\int_0^{2\pi} \int_0^{2\pi} \breve{\omega}\breve{\omega}^* \, dx \, dy]_{N_e}$, with $(\cdot)^*$ representing complex conjugate. Here, $[\cdot]_{N_e}$ represents an averaging across the N_e different realisations of the burst event. Figure 2(*a*) shows the obtained Fourier spectrum. To isolate the quiet region and the burst events, we use distinct sets of frequencies. The blue-shaded frequencies in figure 2(*a*) are used for the quiet region, and the red-shaded frequencies for the burst event. Let us denote the reconstruction of the data using this truncated Fourier basis as $\omega_r(x, y, t)$. Figure 2(*b*) shows the time series of the reconstructions $\langle \omega_r, \omega_r \rangle_{x,y}/D_{lam}$ of the quiet region in blue and the burst event in red. These reconstructions are compared with the full data $\langle \omega, \omega \rangle_{x,y}/D_{lam}$ in black.

The number of modes required for isolating the different regions is identified by defining an error $\epsilon(t)$ in the projection of $\omega_r(x, y, t)$ onto $\omega(x, y, t)$, where $\epsilon(t) := 1 - \langle \omega_r, \omega \rangle_{x,y}/\langle \omega, \omega \rangle_{x,y}$. Let $[\cdot]_t$ denote averaging in time. The blue-shaded frequencies in figure 2(*a*) ensure that $[\epsilon(t_q)]_t < 0.2$ where t_q is defined as the times t when $D(t)/D_{lam} \leq 0.1$, i.e. the quiet region. Similarly, the red-shaded frequencies in figure 2(*a*) ensure that $[\epsilon(t_b)]_t < 0.4$, where t_b is defined as the times t when $D(t)/D_{lam} \geq 0.15$, i.e. the burst event. The numerical values of $[\epsilon(t_q)]_t < 0.2$ and $[\epsilon(t_b)]_t < 0.4$ simply ensure that the dominant frequencies (or wavelets, as in the next section) are included, and changing the values does not significantly impact any of the discussions in this work (see Appendix C).

From figure 2(*b*), we find that the Fourier basis is not able to efficiently isolate the burst event, because the red line does not go to zero in the quiet regions of the flow. Additionally, we require a significant number of frequencies to reconstruct the burst event. This is expected since we are trying to represent a localised event using the Fourier basis
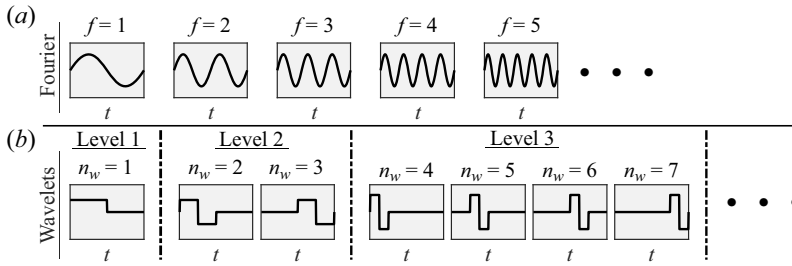
Figure 3. Schematic showing (*a*) the Fourier basis and (*b*) the discrete wavelet basis of Daubechies 1. The vertical dashed-dot lines in (*b*) demarcate the different levels of the wavelet basis, and will be used again in figure 5(*a*) when plotting the energy of the wavelet coefficients.

that is global. In order to remedy these problems, in the next section we will explore using a localised basis – wavelets – for this purpose.

3.2. *Daubechies 1 wavelet basis and wavelet transform*

We now employ a wavelet basis to capture the burst events. The discrete Daubechies 1 (DB1) wavelet, which is also referred to as the Haar wavelet, will be used for a majority of this work. The only exception is Appendix B, where for a different choice of wavelets, that of Daubechies 2, we see that the discussions in this work remain similar.

To obtain a wavelet basis $\Theta_{n_w}(t)$, we first make a choice of the wavelet corresponding to $n_w = 1$, i.e. $\Theta_1(t)$, which is the mother wavelet. For the Daubechies 1 wavelet basis used in this work, the mother wavelet is a step function, as shown in the first panel of figure 3(*b*). The mother wavelet covers the entire time domain, and here we denote this mother wavelet as belonging to level 1 of the wavelet basis. To get level 2 of this wavelet basis, the mother wavelet is compressed by half. Now we need two wavelets to cover the entire domain, and these are shown as $n_w = 2$ and $n_w = 3$ in figure 3(*b*). Level 3 consists of the mother wavelet compressed by a factor of four, and then repeated four times to cover the domain. This level is shown as $n_w = 4$–7 in figure 3(*b*). The vertical black dashed-dot lines in figure 3(*b*) demarcate the different levels of the wavelet transform. Throughout this manuscript, we use such vertical black dashed-dot lines to demarcate the levels. (It should be noted that, in practice, there is a level 0 corresponding to $n_w = 0$ that contains the lowest frequencies of the data that are not included in the other levels. In more technical terms, the wavelet transform for $N = 200$ includes the 'detail coefficients' from 7 levels of the transform as well as the 'approximation coefficient' from level 1 (see Daubechies 1988).) We see that, when considering wavelets, there are two factors that are important: (i) the compression of the wavelet, which is related to the concept of frequency in the Fourier domain and (ii) the location of the wavelet in time.

Similar to the Fourier transform in § 3.1, we obtain a wavelet transform of $\omega(x, y, t)$ as

$$\omega(x, y, t) = \sum_{n_w=0}^{N_w} \hat{\omega}(x, y; n_w)\Theta_{n_w}(t), \qquad (3.2)$$

where ($\hat{\ }$) represents the transform onto the basis Θ_{n_w}, which is here the wavelet basis. The energy of the wavelet coefficients can then be obtained as $E_\omega(n_\omega) = [\int_0^{2\pi} \int_0^{2\pi} \hat{\omega}\hat{\omega}^* \, dx \, dy]_{N_e}$. It should be noted that the $\Theta_{n_w}(t)$ used in this work is real valued. However, since it is a complete basis, it provides a basis for both real-valued and
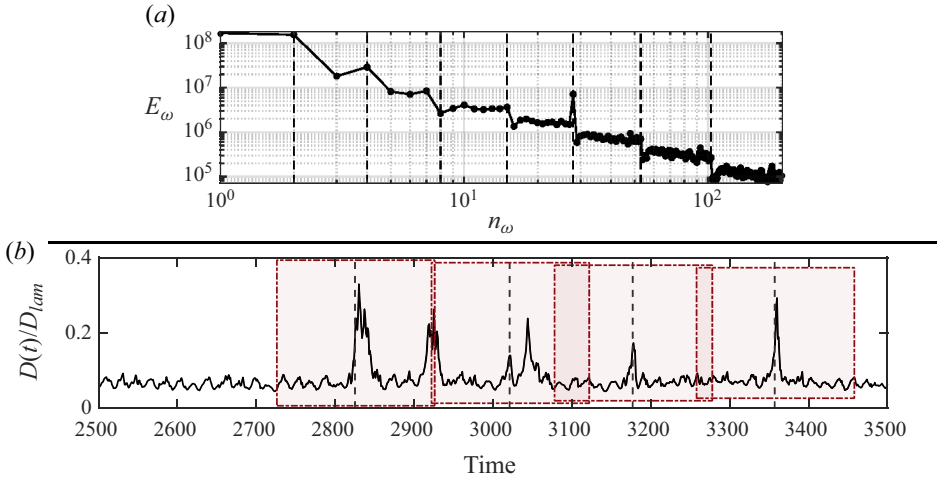
Figure 4. (*a*) The ensemble-averaged energy of the wavelet coefficients is shown for the case when ensembles are chosen as consecutive time blocks. (*b*) A different strategy for choosing ensembles is also illustrated, where the window is chosen such that a burst lies at the centre of it.

complex-valued data. This is relevant when we later consider the wavelet transform of the 1-D Fourier-transformed (in the *x*-direction) data.

A wavelet transform requires a choice of boundary conditions and throughout this manuscript, periodic boundary conditions have been used. The WPOD described later gives similar results for other physically relevant boundary conditions, such as symmetric and reflecting boundary conditions.

3.3. *Burst centred windowing*

Before looking at the energy of the wavelet coefficients, let us briefly discuss the choice of the N_e realisations of the burst event. Generally, to obtain the different ensembles for ensemble averaging, we split the available data into several consecutive data blocks of equal length, and compute the spectrum for each of these ensembles. The spectra are then averaged across the ensembles. The energy of the wavelet coefficients obtained from such consecutive ensembles is shown in figure 4(*a*). Within each of the levels (indicated by the vertical dashed-dot lines), we see that there are no noticeable trends, and peaks are notably absent. This absence of peaks can be explained by recalling that the location in time is important when considering wavelets. In this case, for each ensemble, the burst events occur at different locations in time and therefore appear at different n_w.

To remedy this, we here adopt the alternative windowing strategy that was briefly mentioned in § 3.1 and is depicted in figure 4(*b*). A realisation of the burst event is defined using the start of a burst event T_b as $T_b - 100 \leq t \leq T_b + 100$, where T_b is identified using the condition $D(t)/D_{lam} \geq 0.15$ (note, time is here non-dimensionalised by $\sqrt{L_y/2\pi\zeta}$). As in § 3.1, here, we consider $N_e = 50$ realisations of the burst event, each containing $N_t = 200$ time snapshots of vorticity $\omega(x, y, t)$ spaced apart by time $dt = 1$. The spectrum obtained from this new windowing strategy is shown in figure 5(*a*). From the red-shaded regions of the spectrum in figure 5(*a*), we observe clear peaks that are present because of the burst events. In the next section, we will more clearly show that these peaks correspond to the burst events.
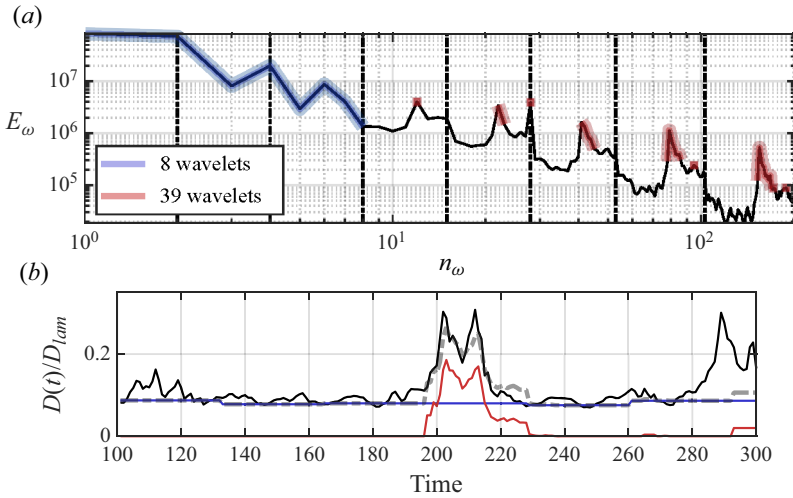
Figure 5. (*a*) The ensemble-averaged energy of the wavelet coefficients is shown in black, and the wavelets used to reconstruct the separate regions in (*b*) are shaded in different colours: the 8 wavelets for the quiet region are shaded in blue and the 39 wavelets for the burst event are in red. The vertical dashed lines indicate the different levels of the wavelet transform (see figure 3). (*b*) The full data for $k_x = 0, 1, 2, 3$ (black) are compared with the reconstructions (using the shaded frequencies in (*a*)) of the quiet region (blue) and the burst event (red). For comparison, the grey dashed-dot line shows the sum of the blue and the red lines.

3.4. *Decomposing the flow: wavelet bases*

The number of levels present in the spectrum is determined by the length of the time window (here $T = 200$) and the type of wavelet used (here DB1). In figure 5(*a*) there are 8 levels that are demarcated by the vertical dashed-dot lines. We here use distinct sets of wavelets to isolate the quiet region and the burst events. The first 3 levels will be used to reconstruct the quiet region, and these are shaded in blue. Next, 20 % of the most energetic modes in levels 4–8 will be used to reconstruct the burst event, and these are shaded in red (Appendix C shows the insensitivity of the results presented to this specific choice of 20 % of the wavelets). As in § 3.1, the number of wavelets used to reconstruct the flow is chosen such that the error $[\epsilon(t_q)]_t < 0.2$ and $[\epsilon(t_b)]_t < 0.4$ (see § 3.1 for the definition of the error metric). Let us denote the data reconstructed using a truncated wavelet basis as $\omega_r(x, y, t)$. Figure 5(*b*) shows the time series of the reconstructions $\langle \omega_r, \omega_r \rangle_{x,y}/D_{lam}$ of the quiet region in blue and the burst event in red. The reconstructions are compared with the full data $\langle \omega, \omega \rangle_{x,y}/D_{lam}$ in black. We observe that isolating the quiet region and the burst events is approximately possible using wavelets.

In comparing the wavelet-based reconstruction in figure 5(*b*) with the Fourier-based reconstruction in figure 2(*b*), three observations stand out. Firstly, and most importantly, wavelets are able to isolate the burst events better than the Fourier basis. To understand why, let us turn our attention to the relatively small magnitude (relative to the burst events) oscillations in the quiet region of the flow. When considering the Fourier basis, the same Fourier frequencies contribute both to these quiet oscillations and the burst events. However, since these oscillations occur at different locations in time relative to the burst events, the wavelet basis is able to produce reconstructions of the burst event uncontaminated by the quiet oscillations. Secondly, to reconstruct the burst event, fewer wavelets are required in comparison with Fourier frequencies: 39 wavelets as opposed to 108 (54 positive) Fourier frequencies. Finally, from figure 5(*b*) we see that wavelets are able to isolate a single burst event, in contrast to the Fourier-based reconstruction in

figure 2(*b*) where both the burst events are captured equally. Therefore, isolating single burst events, when there are multiple similar events present in a time window, is only possible using the wavelets bases.

We can therefore conclude that wavelets are better at isolating burst events. Using wavelets, we are able to obtain a signal of the burst event that is uncontaminated by the oscillations in the quiet region. Additionally, wavelets enable a lower-order representation of the burst event by requiring fewer wavelets (than Fourier frequencies) to reconstruct the burst event. In the next section, we will therefore concentrate on using the wavelet basis to probe the flow patterns active in the quiet region and the burst events.

4. Prediction method 1: WPOD based

Proper orthogonal decomposition, introduced by Lumley (1967, 1970), is a common technique employed to find the flow patterns that are energetically dominant. In this section, we consider two POD-based methods that use a wavelet basis: (i) WPOD (§§ 4.1 and 4.2) and (ii) its variation composite-WPOD (§ 4.3). The aim of these methods is the identification of the coherent structures in an intermittent flow. Here, a coherent structure is defined as a flow pattern that maintains a significant degree of correlation with itself over a range of space and time (Robinson 1991). After identifying the flow patterns, we use them to predict the burst events (§§ 4.4 and 4.5).

4.1. *A description of WPOD*

Many adaptations of POD, tailored for various classes of problems, are found in the literature (for instance, see reviews by Taira *et al.* (2017) and Rowley & Dawson (2017) and references therein). We are here interested in finding structures that are coherent in space and time, and a recently introduced POD-based technique for this purpose is spectral-POD (SPOD) (Towne, Schmidt & Colonius 2018). In this method, the flow is first projected onto a Fourier basis. Thereafter, a POD is performed at each Fourier frequency that gives coherent structures at that particular frequency. These structures are coherent in space due to the properties of POD and coherent in time since they are Fourier modes. However, in § 3.4, we saw that a wavelet basis is better at characterising intermittent flows. Therefore, instead of a SPOD, here we use a WPOD. Using this method we obtain structures that are coherent in space, and both coherent and localised in time since they are wavelet coefficients.

Before describing WPOD, to provide context, let us briefly consider the regular POD. In this case, we have velocity fields $q(x, y, t) = (u(x, y, t), v(x, y, t))$ for a range of time. (For POD, we are required to choose a norm that is maximised to obtain the POD modes. Kinetic energy is a physically relevant norm, and choosing velocity as data, instead of vorticity, ensures that the kinetic energy is used as the POD norm.) The POD modes $\phi_i(x, y)$ give an orthogonal basis for $q(x, y, t)$, such that the 1st POD mode captures the largest variance of the data, the *i*th POD mode captures the *i*th largest variance, and so on. In other words, if $\mathcal{E}_i^{pod}$ is the projection of the data $q(x, y, t)$ onto the *i*th POD mode, $\phi_i(x, y)$

$$\mathcal{E}_i^{pod} = \frac{[|\langle q(x, y, t), \phi_i(x, y)\rangle_{x,y}|^2]_t}{\langle \phi_i(x, y), \phi_i(x, y)\rangle_{x,y}}, \tag{4.1}$$

then $\mathcal{E}_i^{pod} > \mathcal{E}_{i+1}^{pod}$. Here, as before, $[\cdot]_t$ denotes averaging in time, $\langle a, b\rangle_{x,y}$ denotes the inner product $\int_0^{L_y} \int_0^{L_x} b^*(x, y, t)a(x, y, t) \, dx \, dy$ and $|\cdot|$ represents absolute value. The problem

of finding POD modes reduces to finding the eigenvalues of the correlation matrix QQ^* where Q is a matrix with columns containing $q(x, y, t)$, i.e. the 1st column of Q is $q(x, y, t_1)$ and the ith column is $q(x, y, t_i)$. The eigenvectors of QQ^* are equivalently the left singular vectors of the matrix Q, and therefore the problem can be solved by performing a singular value decomposition (SVD) of the data matrix Q.

Rather than finding the coherent structures in the entire flow using POD, we are interested in finding the coherent structures at particular wavelets. Let us therefore consider wavelet-POD. For this, first consider the N_e different realisations of the burst event (see § 3.3 for how each realisation is chosen from the data). From these N_e realisations, consider one realisation n_e, where now $1 \leq n_e \leq N_e$. At this n_e, we have the data $q(x, y, t; n_e) = (u(x, y, t; n_e), v(x, y, t; n_e))$. A wavelet transform of this n_eth realisation of the burst event will give us $\hat{q}(x, y; n_w, n_e) = (\hat{u}(x, y; n_w, n_e), \hat{v}(x, y; n_w, n_e))$, where $\hat{u}$ and $\hat{v}$ represent the wavelet transform of u and v. Therefore, for each wavelet n_w, and from each realisation of the burst event n_e, we have the state vector $\hat{q}(x, y; n_w, n_e)$. If we now concentrate on just one wavelet n_w, we have N_e data vectors $\hat{q}(x, y; n_w, 1 : N_e)$.

The objective now is to find basis vectors $\hat{\phi}_i(x, y; n_w)$ such that

$$\hat{q}(x, y; n_w, n_e) = \sum_{i=0}^{N_e} a_i(n_w, n_e)\hat{\phi}_i(x, y; n_w). \tag{4.2}$$

For each n_w, the equivalent of the POD energy in (4.1) now becomes

$$\mathcal{E}_i^{wpod}(n_w) = \frac{[|\langle \hat{q}(x, y; n_w, n_e), \hat{\phi}_i(x, y; n_w)\rangle_{x,y}|^2]_{n_e}}{\langle \hat{\phi}_i(x, y; n_w), \hat{\phi}_i(x, y; n_w)\rangle_{x,y}}, \tag{4.3}$$

where $\mathcal{E}_i^{wpod}(n_w) \geq \mathcal{E}_{i+1}^{wpod}(n_w)$. It should be noted that, unlike in (4.1) where the averaging is over time, in (4.3) the averaging is across the N_e different realisations of the burst event (denoted by $[\cdot]_{n_e}$). If we consider the WPOD modes across all n_w and pick the dominant mode, i.e. the mode with maximum energy across n_w, then the projection that is maximised is

$$\max_{n_w}(\mathcal{E}_1^{wpod}(n_w)) = \frac{[|\langle q(x, y, t; n_e), \phi_1(x, y, t)\rangle_{x,y,t}|^2]_{n_e}}{\langle \phi_1(x, y, t), \phi_1(x, y, t)\rangle_{x,y,t}}, \tag{4.4}$$

where $\langle a, b\rangle_{x,y,t}$ denotes the inner product $\int_0^T \int_0^{L_y} \int_0^{L_x} b^*(x, y, t)a(x, y, t)\,dx\,dy\,dt$. Here, $\phi_i(x, y, t)$ represents the WPOD mode $\hat{\phi}_i(x, y; n_w)$ in time, i.e. $\phi_i(x, y, t)$ is an inverse wavelet transform of $\hat{\phi}_i(x, y; n_w)$. Similar to POD, for WPOD we perform a SVD of the data matrix $\hat{Q}_{n_w}$, where columns of $\hat{Q}_{n_w}$ are the data $\hat{q}(x, y; n_w, 1 : N_e)$. The ith left singular vector is the ith WPOD mode, and the square of the ith singular value is the corresponding WPOD energy $\mathcal{E}_i^{wpod}(n_w)$ (4.3).

4.2. *The WPOD-based analysis of the 2-D Kolmogorov flow*

Figure 6(*a*) shows the WPOD energies $\mathcal{E}_i^{wpod}(n_w)$ (4.3) as a function of wavelet n_w. In other words, each vertical line in figure 6(*a*) corresponds to the WPOD obtained at that particular n_w. Let us first focus on the wavelets responsible for the quiet region shaded in blue, i.e. the first three levels of the wavelet transform. Notably, only these lower levels show any appreciable low-rank behaviour, i.e. within these levels the first few WPOD modes capture significantly more energy than the higher modes. Low rankness in the WPOD spectrum
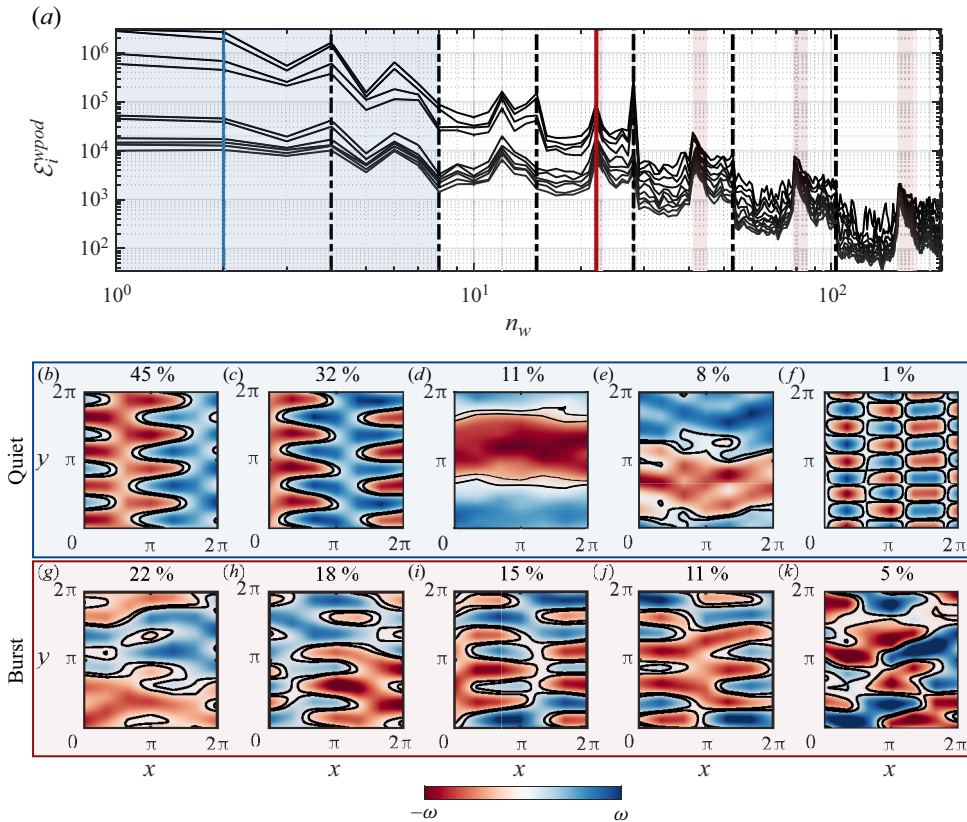
Figure 6. (*a*) The WPOD spectrum is shown as a function of wavelet n_w. The energies of the first 10 WPOD modes are shown. The vertical dashed-dot lines demarcate the levels of the wavelet transform. The shaded regions represent the wavelets that are responsible for the quiet region in blue and the burst event in red. The first 5 WPOD modes are shown for two different wavelets: (*b–f*) $n_w = 2$ responsible for the quiet region marked by the blue vertical line in (*a*) and (*g–k*) $n_w = 22$ responsible for the burst event marked by the red vertical line in (*a*).

suggests that there is an energetically dominant mechanism that is responsible for the quiet region of the flow. To probe this further, let us now look at the WPOD modes at $n_w = 2$ in figure 6(*b–f*). The WPOD modes 1 and 2, as well as modes 3 and 4, are shifted versions of the same mode, a result of the inherent symmetries in the flow. (While symmetries can be incorporated into the POD modes, the instantaneous fluctuations of the flow do not adhere to these symmetries, and so we present modes without symmetrisation). Together, modes 1 and 2 account for 77 % of the energy at this n_w. Crucially, these first two modes closely resemble the unstable eigenfunction obtained from the Navier–Stokes equations linearised around the mean flow (see Appendix A). This indicates that this unstable eigenfunction is mainly responsible for the quiet region of this flow. This is consistent with the observations in Farazmand & Sapsis (2017), where they employed an alternative strategy to capture this unstable eigenfunction, and used it to predict the burst events. Moving on to modes 3 and 4, while these modes are energetically significant, they capture less energy compared with modes 1 and 2. Together they capture 19 % of the energy at this n_w. Structurally, modes 3 and 4 capture shearing motions.

Let us now turn our attention to the wavelets responsible for the burst event. These wavelets are shaded in red in figure 6(*a*). One initial observation is that there is no significant low rankness at a majority of these wavelets. This lack of low rankness generally suggests that there is no one dominant mechanism that is responsible for the burst event. To investigate these modes further, consider the WPOD modes at $n_w = 22$ in figure 6(*g*–*k*). Notably, the first 4 WPOD modes in the burst event are structurally similar to the modes in the quiet region. Additionally, we observe that modes 2–4, while being similar to the unstable eigenfunction, are fragmented versions of this eigenfunction. It should be noted that, this fragmentation of the modes is more apparent for certain n_w in the burst region (for instance, it is not as clearly apparent for $n_w = 12$ in level 4). Therefore, for a more conclusive illustration of these fragmented modes, we will consider composite-WPOD modes in the next section.

From these observations, we can hypothesise that the shearing motions are responsible for disrupting the flow due to the unstable eigenfunction. Intermittently, this shearing disrupts the flow enough to cause a burst event. While a WPOD analysis can suggest that such a mechanism causes the burst events, to conclusively show this, we need to do a dynamic mode decomposition (Schmid 2022) analysis that identifies the relevant instabilities of the flow generated by the unstable eigenfunction. However, this falls beyond the scope of the current manuscript.

4.3. *Coherent structures in quiet and burst regions – a composite-WPOD analysis*

In this section, we introduce composite-WPOD. Instead of identifying structures at specific wavelets n_w as done for WPOD in the previous section, in composite-WPOD we identify the coherent structures for a set of wavelets $\{n_{w1}, n_{w2}, \ldots\}$. This is important since, from § 3.4 we know that, rather than individual wavelets, sets of wavelets contribute to the quiet region and the burst events. For example, to find modes for the quiet region, we need modes that represent the set of wavelets $\boldsymbol{n}^q = \{n_{w1}^q, n_{w2}^q, \ldots n_{wN_q}^q\}$ that are responsible for the quiet region (represented by the blue-shaded values of n_w in figure 6*a*). We therefore use a composite version of the WPOD used in § 4.1.

In § 4.1, to obtain the WPOD modes, we computed the SVD of a data matrix $\hat{Q}_{n_w}$. The columns of $\hat{Q}_{n_w}$ were taken to be the data $\hat{\boldsymbol{q}}(x, y; n_w, 1 : N_e)$, such that the 1st column corresponds to $\hat{\boldsymbol{q}}(x, y; n_w, 1)$, the ith column to $\hat{\boldsymbol{q}}(x, y; n_w, i)$, and so on. Here, we instead consider the data matrix $\hat{P}$ that contains coefficients at all the n_w that is contained in $\boldsymbol{n}^q$ such that

$$\hat{P} = [\hat{\boldsymbol{q}}(x, y; n_{w1}^q, 1), \ldots, \hat{\boldsymbol{q}}(x, y; n_{w1}^q, N_e), \ldots \hat{\boldsymbol{q}}(x, y; n_{wi}^q, 1), \ldots, \hat{\boldsymbol{q}}(x, y; n_{wi}^q, N_e), \ldots]. \tag{4.5}$$

In effect, to obtain $\hat{P}$, we horizontally stack all the N_q number of $\hat{Q}_{n_w}$ that correspond to the n_w in $\boldsymbol{n}^q$, i.e. $\hat{P} = [\hat{Q}_{n_{w1}^q}, \hat{Q}_{n_{w2}^q}, \ldots, \hat{Q}_{n_{wi}^q}, \ldots]$. The SVD of $\hat{P}$ will give us the dominant structures that are responsible for the set of wavelets $\boldsymbol{n}^q$.

We denote the composite-WPOD energies for wavelets $\boldsymbol{n}^q$, obtained as the square of the singular values of $\hat{P}$, as $\mathcal{E}_i^q$. In other words, $\mathcal{E}_1^q$ is the energy of the dominant composite-WPOD mode that captures the dynamics across the set of wavelets $\boldsymbol{n}^q$. (To clarify the notation for the POD norms used in this section, we used $\mathcal{E}^{pod}$ for the POD norm, $\mathcal{E}^{wpod}$ for the WPOD norm and $\mathcal{E}$ for the composite-WPOD norm.) The first few such composite-WPOD modes for the set of wavelets $\boldsymbol{n}^q$ are shown in figure 7(*a*–*d*). The percentage energy captured by the mode is also shown in the figure. Similarly,
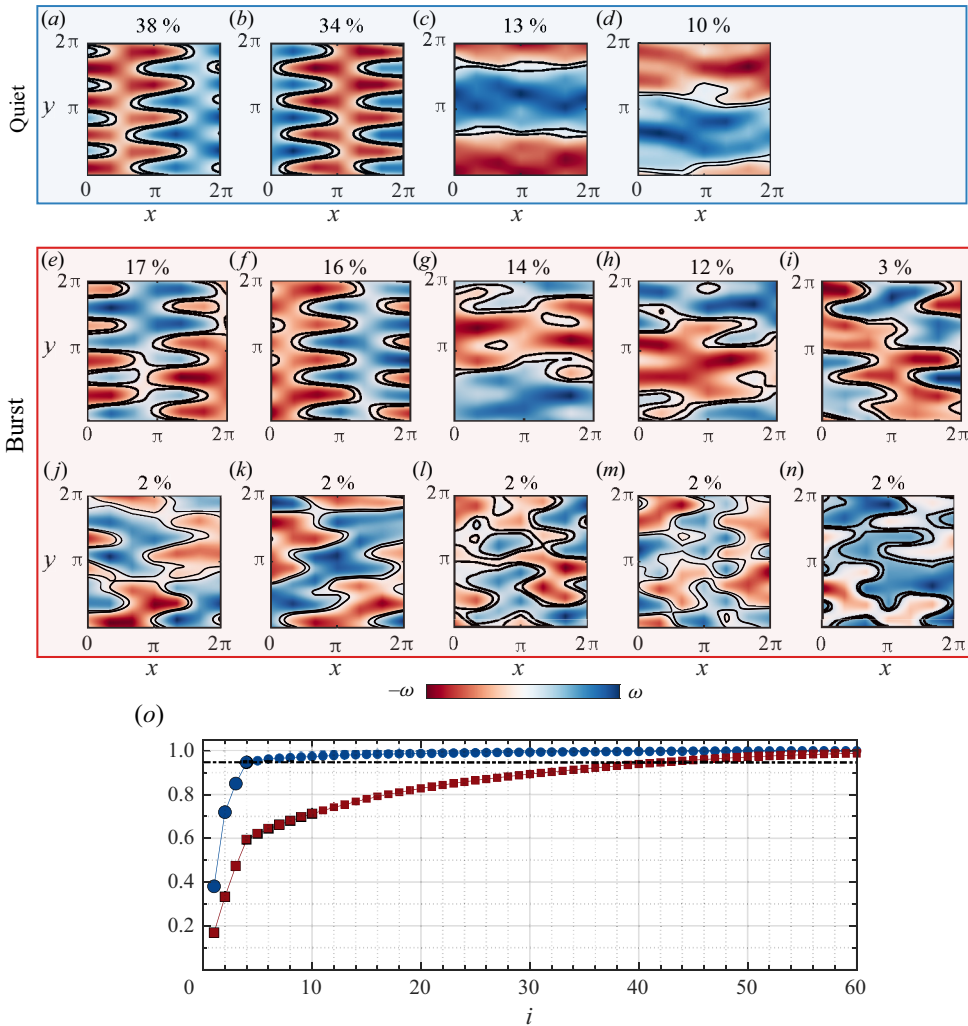
Figure 7. The first few composite-WPOD modes are shown for two different sets of wavelets: (*a–d*) wavelets responsible for the quiet region marked by the blue-shaded region in figures 6(*a*) and 6(*e–n*) wavelets responsible for the burst event marked by the red-shaded regions in figure 6(*a*). The titles of these plots show the percentage energy captured by the mode computed as $100 \times \mathcal{E}_i^q / \sum_{j=0}^{M} \mathcal{E}_j^q$ for the quiet region, and similarly for the burst events. (*o*) Also shown is the cumulative contribution of the first i modes to the total energy for the quiet regions computed as $(\sum_{j=0}^{i} \mathcal{E}_j^q)/(\sum_{j=0}^{M_q} \mathcal{E}_j^q)$ (blue line, circle markers) and the burst events computed as $(\sum_{j=0}^{i} \mathcal{E}_j^b)/(\sum_{j=0}^{M_b} \mathcal{E}_j^b)$ (red line, square markers).

composite-WPOD modes can be obtained for the wavelets $\boldsymbol{n}^b$ that contribute to the burst events, and here we denote the WPOD energies of these modes as $\mathcal{E}_i^b$. The first 10 among these WPOD modes for the burst event are shown in figure 7(*e–n*). Figure 7(*o*) shows the cumulative contribution of the first i modes to the total energy. In other words, the blue line in figure 7(*o*) shows $(\sum_{j=0}^{i} \mathcal{E}_j^q)/(\sum_{j=0}^{M_q} \mathcal{E}_j^q)$, where $M_q = N_e \times N_q$ is the total number of composite-WPOD modes obtained for the set of wavelets $\boldsymbol{n}^q$ for the quiet region. The red line shows the same quantity for the $M_b = N_e \times N_b$ composite-WPOD modes, corresponding to the set of wavelets $\boldsymbol{n}^b$ for the burst event. In this study $N_e = 50$, $N_q = 8$

and $N_b = 39$ (see figure 5a), and therefore $M_q = 400$ and $M_b = 1950$. The horizontal dashed-dot line in figure 7(o) indicates 95 %.

Let us first focus on the quiet region. From the blue line in figure 7(o) we see that the curve very quickly approaches the dashed-dot line indicating 95 %. The first four modes capture most of the energy of the flow. These four modes are shown in figure 7(a–d), and they can be compared with their counterparts in figure 6(b–e). We note that the leading modes obtained from both WPOD versions are similar. Consistent with the observations from figure 6, composite-WPOD modes 1 and 2 correspond to the unstable eigenfunction and modes 3 and 4 represent shearing motions in the *y*-direction. (The modes in figure 7 exhibit greater convergence compared with those in figure 6 due to the inclusion of data from a collection of n_w, thereby increasing the input data used.)

Now consider the burst region. From the red line in figure 7(o), we see that the increase in total energy is more gradual. The first four modes, shown in figure 7(e–h), still capture a considerable part of the energy. Structurally, these four modes resemble the modes in the quiet region. This is consistent with the observation in § 4.2, and shows that the dominant modes in the quiet region persist during the burst events as well. In effect, this flow cannot be precisely divided into the quiet region and the burst events. However, going back to figure 7(o), the red line shows a very slow increase, and many suboptimal modes are required to reach 95 % energy (the horizontal dashed-dot line). Therefore, although these suboptimal modes (i.e. mode 5 and onward) each contribute very little energy, large numbers of them together play a significant role in the burst events. A few of these modes are shown in figure 7(i–n). The leading among these modes appear to be modified, here sheared, versions of the unstable eigenfunction (see for example figures 7(i), 7(j) and 7(k)). This is also consistent with the observations in § 4.2. Notably, such fragmented and sheared versions of the unstable eigenfunction are modes that are typical to the burst events.

4.4. *Tracking composite-WPOD modes in a time series*

So far, we have identified coherent structures that exist in the quiet region and the burst events. In this section, we track these coherent structures in a time series obtained from the flow. In other words, we are interested in analysing how the contributions of these coherent structures to the flow evolve with time. This will pave the way for the discussion in the next section (§ 4.5), where we will use these coherent structures to introduce the WPOD-based method for predicting the burst events.

We have two sets of composite-WPOD modes: (i) let L_q represent the set of $M_q = N_e \times N_q$ number of composite-WPOD modes corresponding to the quiet region with the *j*th mode in L_q having WPOD energy $\mathcal{E}_j^q$ and similarly (ii) let L_b represent the set of $M_b = N_e \times N_b$ modes for the burst event with energies $\mathcal{E}_j^b$. Consider the modes $\boldsymbol{\phi}_j^q(x, y)$ ($j = 1, \ldots, M_q$) from L_q. Now consider a time series $\boldsymbol{q}(x, y, t)$ obtained from flow, where $\boldsymbol{q} = (u, v)$ is the state vector. Note that $\boldsymbol{q}(x, y, t)$ can be a time series of arbitrary length with any number of burst events occurring at any point in time. Additionally, $\boldsymbol{q}(x, y, t)$ could lie outside the time window used to obtain the N_e realisations of the burst event for WPOD (as required for the problem of predicting the burst events in the next section). At each time t, we aim to assess the presence of the structures $\boldsymbol{\phi}_j^q(x, y)$ in the flow field $\boldsymbol{q}(x, y, t)$. For this, we first compute $E_{qj}(t)$, which is the magnitude of energy shared between a mode $\boldsymbol{\phi}_j^q(x, y)$ and $\boldsymbol{q}(x, y, t)$ as

$$E_{qj}(t) := \int_{k_y} \int_{k_x} |FT_{xy}(\boldsymbol{q})(k_x, k_y; t) FT_{xy}(\boldsymbol{\phi}_j^q)(k_x, k_y; t)^*|^2 \, \mathrm{d}k_x \, \mathrm{d}k_y. \qquad (4.6)$$
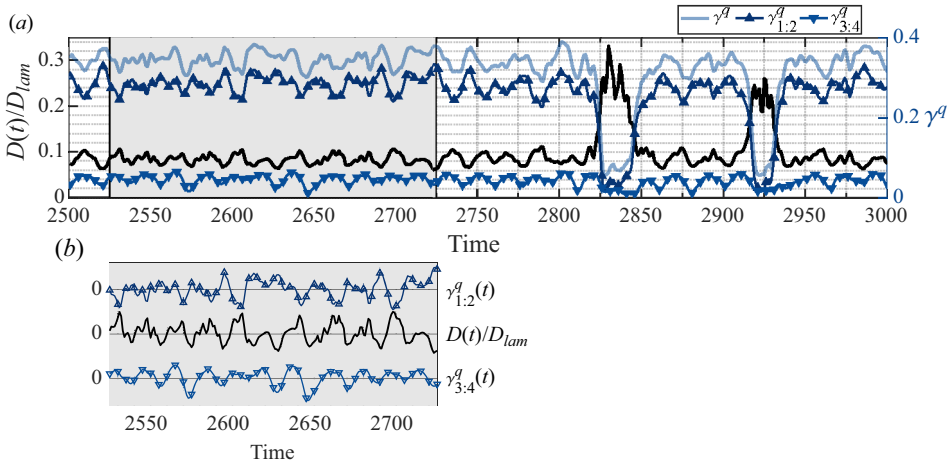
Figure 8. (*a*) Tracking coherent structures for the quiet region using γ^q (blue line). Two components of γ^q are also shown: $\gamma_{1:2}^q(t)$ ($\triangle$) and $\gamma_{3:4}^q(t)$ ($\triangledown$). (*b*) Also shown are the mean-removed and normalised profiles of $D(t)/D_{lam}$, $\gamma_{1:2}^q(t)$ and $\gamma_{3:4}^q(t)$ for the time window indicated by the grey-shaded box in (*a*).

Here, $FT_{xy}(\cdot)$ represents the 2-D Fourier transform in the spatial directions, and k_x and k_y are the wavenumbers in the x and y-directions, respectively. We normalise $E_{qj}(t)$ using (i) $E_{jj} := \langle \boldsymbol{\phi}_j^q, \boldsymbol{\phi}_j^q \rangle_{x,y}$ which is the energy of $\boldsymbol{\phi}_j^q(x, y)$ and (ii) $E_{qq}(t) := \langle \boldsymbol{q}, \boldsymbol{q} \rangle_{x,y}$ which is the energy of $\boldsymbol{q}(x, y, t)$.

The coherence $\gamma^q(t)$ between $\boldsymbol{q}(x, y, t)$ and the modes in L_q can now be defined as

$$\gamma_j^q(t) = \frac{E_{qj}(t)}{E_{qq}(t)E_{jj}}, \quad \gamma^q(t) = \sum_{j=1}^{M_q} \left(\frac{\mathcal{E}_i^q}{\sum_{j=0}^{M_q} \mathcal{E}_j^q} \right) \gamma_j^q(t). \quad (4.7a,b)$$

Here, $\gamma_j^q(t)$ is the coherence between a point in the time series from the flow $\boldsymbol{q}(x, y, t)$ and the jth composite-WPOD mode in L_q. The value of $\gamma_j^q(t)$ is bounded in the range $0 \leq \gamma_j^q(t) \leq 1$, with 0 indicating no coherence between $\boldsymbol{\phi}_j^q(x, y)$ and $\boldsymbol{q}(x, y, t)$ and 1 indicating perfect coherence. Hence, $\gamma^q(t)$ is the weighted average of the coherence across the M_q different modes in L_q, weighted by the fraction of energy that each mode contributes to the energy of the quiet region. The value of $\gamma^q(t)$ therefore also lies between 0 and 1, where 0 indicates that the modes in L_q are not present in $\boldsymbol{q}(x, y, t)$ at that time t and 1 indicates that the modes in L_q are the only structures present in $\boldsymbol{q}(x, y, t)$. Similarly, we can also define $\gamma^b(t)$ as the average coherence of $\boldsymbol{q}(x, y, t)$ with structures in L_b. It should be noted that, the actual value of $\gamma^q(t)$ and $\gamma^b(t)$ do not hold physical significance. Instead, our interest is in the trends of $\gamma^q(t)$ and $\gamma^b(t)$ over time. Let us first consider $\gamma^q(t)$ for a sample time series. Figure 8(*a*) displays $\gamma^q(t)$ in blue, along with the time series of $D(t)/D_{lam}$ in black. To obtain a smoother curve, the average of $\gamma^q(t-2)$, $\gamma^q(t-1)$ and $\gamma^q(t)$ is computed at each time t. Similar averaging is also later carried out for $\gamma^b(t)$ (at each time t_1, only values $t \leq t_1$ are used for this averaging). Looking at $\gamma^q(t)$ we observe that: (i) within the quiet region, $\gamma^q(t)$ remains relatively high and (ii) $\gamma^q(t)$ plummets down when burst events occur. It is evident that $\gamma^q(t)$ exhibits distinctive changes in its trends during a burst event. This is consistent with the observations in the literature that shows that the occurrence of a burst event is correlated with how near or far the flow is from equilibrium solutions of
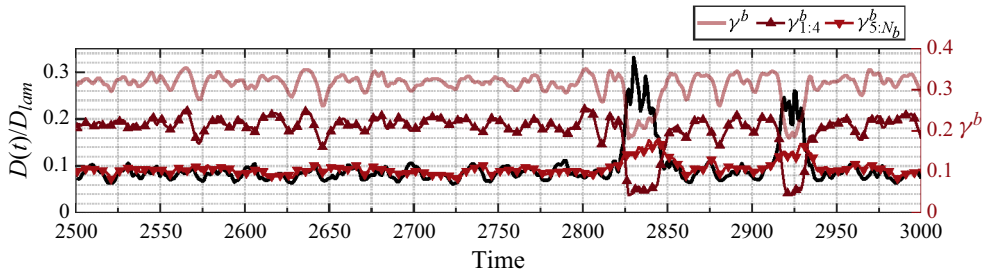
Figure 9. Tracking coherent structures for the burst events using γ^b (red line). Two components of γ^b are also shown: $\gamma_{1:4}^b(t)$ ($\triangle$) and $\gamma_{5:N_b}^b(t)$ (∇).

the flow (Farazmand 2016; Page *et al.* 2021). Looking ahead to the problem of predicting the burst events, $\gamma^q(t)$ should, therefore, become a valuable tool.

To further probe this, figure 8(*a*) also shows two components of $\gamma^q(t)$: (i) $\gamma_{1:2}^q(t)$, which shows the weighted average of the coherence of just the first two modes in L_q, i.e. the unstable eigenfunction (modes in figure 7*a,b*) and (ii) $\gamma_{3:4}^q(t)$, which is the weighted average coherence of modes 3 and 4, i.e. the shearing motions. (modes in figure 7*c,d*). The first significant observation is that $\gamma_{1:2}^q(t)$ closely follows the trends of $\gamma^q(t)$. This is not surprising given that, together, modes 1 and 2 capture more than 70 % of the energy of the quiet region (as seen in figure 7). Therefore, we can say that the trends of $\gamma^q(t)$ are most significantly impacted by the flow due to modes 1 and 2, i.e. the unstable eigenfunction. The second noteworthy observation is that $\gamma_{3:4}^q(t)$ tends to move out of phase with $\gamma_{1:2}^q(t)$. This becomes more evident in figure 8(*b*) where mean-removed and normalised profiles of $D(t)/D_{lam}$, $\gamma_{1:2}^q(t)$ and $\gamma_{3:4}^q(t)$ are shown. The curves are vertically shifted in order to make the trends clearer. From this figure, we see that, when $D(t)/D_{lam}$ increases, the presence of the flow due to the unstable eigenfunction ($\gamma_{1:2}^q(t)$) decreases and that of the shearing structure ($\gamma_{3:4}^q(t)$) increases. This observation provides additional support to our initial hypothesis that the shearing motions disrupt the flow generated by the unstable eigenfunction, thereby increasing dissipation.

Let us now examine $\gamma^b(t)$ for the same time series. Figure 9 shows $\gamma^b(t)$ in red alongside the time-series of $D(t)/D_{lam}$ in black. Upon comparing $\gamma^b(t)$ with $\gamma^q(t)$ in figure 8(*a*), the first apparent observation is that the trends between them are strikingly similar. This observation is consistent with the earlier finding from figure 7, that nearly 60 % of the energy of the burst events is captured by modes that are present in the quiet region. Looking ahead to the problem of predicting the burst events, this similarity between $\gamma^q(t)$ and $\gamma^b(t)$ brings the unfortunate conclusion that the trends of the full $\gamma^b(t)$ may not be useful for prediction. However, our earlier observations showed the existence of suboptimal structures that are unique to the burst events (see figure 7). Presumably, these structures exhibit trends dissimilar to $\gamma^q(t)$. The question, therefore, is whether we can identify a component of $\gamma^b(t)$ that has predictive value?

To explore this further, figure 9 also shows two components of $\gamma^b(t)$: (i) $\gamma_{1:4}^b(t)$ computed using just the first four modes in L_b, i.e. the modes that resemble those from the quiet region (modes in figure 7*e–h*) and (ii) $\gamma_{5:N_b}^b(t)$ computed using modes 5 and onward (the first few of these modes are those in figure 7*i–n*). Two observations become immediately apparent. Firstly, as expected, $\gamma_{1:4}^b(t)$ follow trends similar to the full $\gamma^b(t)$ as well as $\gamma^q(t)$. Secondly, and also more interestingly, $\gamma_{5:N_b}^b(t)$ increases during the burst event. This again shows that these suboptimal modes are unique to the burst events. Again
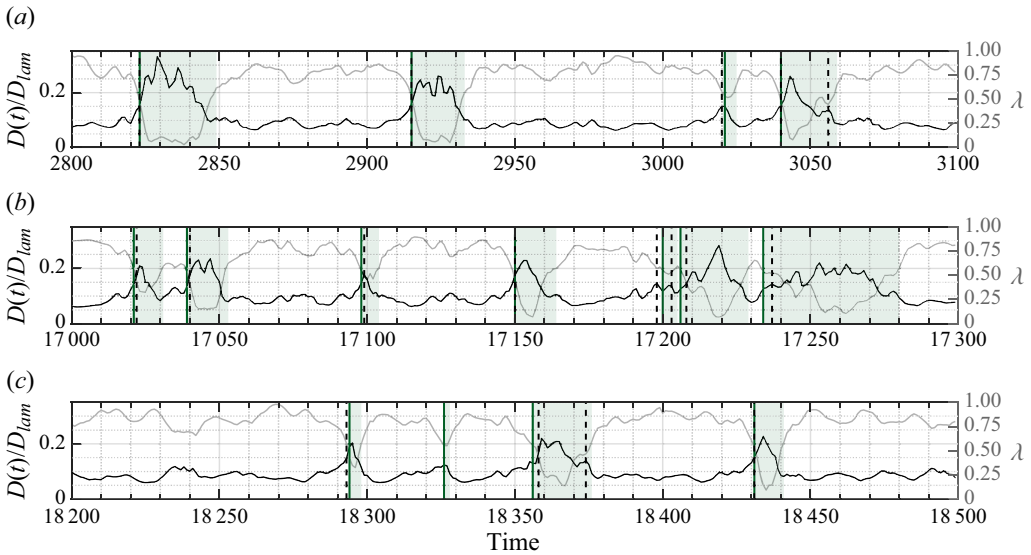
Figure 10. Predictions of the burst events obtained using the WPOD-based method for three separate time series from DNS. The green-shaded regions indicate the identified burst regions, where the predictor λ (grey line) goes below the defined threshold value, i.e. $\lambda < 0.95\lambda_t$. The vertical green lines mark the onset of these burst regions, and therefore represent the predictions of the burst event obtained from the WPOD-based method. Predicted times are compared with the black dashed vertical lines that indicate the predictions obtained from the energy-based method.

looking ahead to the problem of predicting the burst events, these observations show that, although the full $\gamma^b(t)$ may not be helpful in identifying the burst events, the distinctive trends of $\gamma^b_{5:N_b}(t)$ during the burst event will be. (Note, Appendix C shows that it is possible to predict the burst events using just $\gamma^q(t)$, ignoring the trends of $\gamma^b(t)$. However, incorporating the trends of $\gamma^b_{5:N_b}(t)$ does improve the obtained predictions.)

4.5. *Obtaining WPOD-based predictions of burst events*

In this section, to predict burst events, we use the distinctive trends of $\gamma^q(t)$ and $\gamma^b_{5:N_b}(t)$ identified in the previous section. For this purpose, a predictor $\lambda = \gamma^q(t) - \gamma^b_{5:N_b}(t)$ is defined. The average of $\lambda(t-2)$, $\lambda(t-1)$ and $\lambda(t)$ is computed at each time t. Figure 10 shows $D(t)/D_{lam}$ along with the evolution of λ for three different time windows. The time window in figure 10(a) was included among the $N_e = 50$ realisations of the burst events that were used for computing the WPOD modes, while the time windows in figures 10(b) and 10(c) fall outside these N_e realisations. In other words, while the data in figure 10(a) fall within the 'training dataset', figures 10(b) and 10(c) fall outside this training data, and will therefore serve to illustrate the generalisability of the prediction method discussed here. Since we are interested in the trends of λ, and not the magnitudes, we here consider normalised λ (normalised by the minimum and maximum values obtained within a time window $t = 0$–$15\,000$).

From figure 10, we see that λ decreases during burst events. Consequently, we designate a threshold λ_t, and values of λ below λ_t will be identified as burst events. To calculate λ_t, we begin by computing the mean of λ minus the variance, where both these statistics are calculated for time instances that correspond to the quiet regions (i.e. when $D(t)/D_{lam} \leq$

0.1) in the range $t = 0$–$15\,000$. The threshold λ_t is set to be 0.95 times this mean minus the variance. (The impact of varying this coefficient 0.95 to other values will be discussed in § 6.1.) The green-shaded regions in figure 10 mark the times when $\lambda < \lambda_t$, and the solid green vertical lines mark the beginnings of these regions. A majority of these green-shaded regions correspond to burst events. The green vertical lines are therefore the predictions of the burst events obtained using this WPOD-based method.

To assess the prediction performance, the obtained prediction times are here compared with those obtained from a more straightforward strategy of tracking the energy of the flow. In this case, the predictor becomes $\lambda = -D(t)/D_{lam}$ (where the negative sign makes comparison with the wavelet-based predictors more straightforward). Again, the average of $\lambda(t-2)$, $\lambda(t-1)$ and $\lambda(t)$ is computed at each time t. Using the same procedure as for the WPOD-based method, a threshold is computed as 0.95 times the mean of λ minus the variance computed for the quiet region in the range $t = 0$–$15\,000$. The vertical black dashed lines in figure 10 indicate the beginnings of the time windows where the predictor goes below the threshold value. These lines therefore represent the predictions obtained from tracking the energy of the flow, which can directly be compared with the predictions obtained from the WPOD-based method in green.

From figure 10, we see that the WPOD-based method is able to predict the burst events well. However, for this chosen threshold, we obtain false positives, i.e. predictions of oncoming burst events in the absence of such events (e.g. $t \approx 18\,325$ in figure 10c). When compared with the energy-based method, the WPOD-based method does seem to give improved prediction times (see, for instance, $t \approx 17\,235$ and $t \approx 18\,355$ in figure 10). However, we also seem to obtain more false positives from the WPOD-based method.

To quantify the prediction performance, we should consider predictions over long time windows. Here we take a time window of length $T = 20\,000$ and $dt = 1$ outside the N_e realisations used for WPOD (i.e. outside the 'training dataset'), which contains 133 burst events. We compute three quantities. First, the average prediction time τ, which is computed as the difference between the obtained prediction time and the time when the burst begins, i.e. when $D(t)/D_{lam} \geq 0.15$. (Note, τ is shown in units of $\sqrt{L_y/2\pi\zeta}$.) Second, the percentage of predictions that are false positives, denoted by FP%. A false positive is here defined as a prediction where $D(t)/D_{lam}$ of the flow does not go above 0.15. Third, the percentage of false negatives, denoted by FN%. These are instances when the method does not identify a region with $D(t)/D_{lam} \geq 0.15$ as a burst event. Both FP% and FN% are represented as a percentage of the total number of predictions of the burst event obtained from the method. For the WPOD-based method $\tau = 1.06$, FP% $= 20$ and FN% $= 2$, which can be compared with the values for the energy-based method $\tau = 0.36$, FP% $= 13$ and FN% $= 0$. The WPOD-based method has difficulty in capturing burst events that persist for less than 1–2 time units, and these contribute to the very small number of false negatives obtained. From these numbers, we can conclude that the WPOD-based method is capable of predicting burst events with improved prediction times compared with the more straightforward method of tracking energy, albeit with the possibility of slightly increased number of false positives and false negatives.

5. Prediction method 2: wavelet-resolvent analysis based

Up to this point, our focus has been on the coherent structures in the flow. We now shift our attention to the forcing that generates these coherent structures. This will thereafter pave the way for the discussion on the WRA-based prediction method, where we will use the obtained forcing to predict the burst events. To identify this forcing, we use resolvent

analysis. Within the resolvent analysis framework, the nonlinear terms of the linearised Navier–Stokes equations are considered to be a forcing to the linear equations (e.g. Hwang & Cossu 2010; McKeon & Sharma 2010; Moarref *et al.* 2013; Towne, Lozano-Durán & Yang 2020; Morra *et al.* 2021). Using this method, we obtain a complete basis that can be used to represent the flow. Additionally, the method also gives a forcing, i.e. the nonlinear terms, that force the linearised equations to generate the coherent structures.

Conventionally, the resolvent analysis framework is established using a Fourier transform in time. However, here, for precise decomposition of the flow into the quiet and burst regions, we need to use a wavelet basis (see § 3.4). Consequently, to obtain forcing structures for the quiet and the burst regions, we need to use wavelet-based resolvent operators. While a substantial amount of literature considers the Fourier-based resolvent analysis, studies that concentrate on the WRA are limited and very recent (Ballouz *et al.* 2023*a*,*b*). The next section introduces the resolvent operator for a broader range of bases, which includes the Fourier and wavelet bases.

5.1. *Resolvent operator*

To define the resolvent operator, we start with the Fourier-transformed linearised Navier–Stokes equations that were laid out in (2.4) and reproduced here

$$\dot{\tilde{\omega}}(y, t; k_x) + A\tilde{\omega}(y, t; k_x) = \tilde{F}(y, t; k_x). \tag{5.1}$$

Let us consider the basis vectors $\Theta_{n_w}(t)$. We can write $\tilde{\omega}$ in terms of its projection onto this basis as (Farge 1992)

$$\tilde{\omega}(y, t; k_x) = \sum_{n_w=1}^{N_w} \hat{\tilde{\omega}}(y; k_x, n_w)\Theta_{n_w}(t), \tag{5.2}$$

where

$$\hat{\tilde{\omega}}(y; k_x, n_w) = \int_0^T \tilde{\omega}(y, t; k_x)\Theta_{n_w}^*(t)\, \mathrm{d}t. \tag{5.3}$$

We can similarly obtain the coefficients $\hat{\tilde{F}}(y; k_x, n_w)$ of $\tilde{F}(y, t; k_x)$. Here, T is the length of the time window used. For the case considered here, T (here $T = 200$) is the length of a realisation of the burst event that we used for WPOD (see § 3.3). Please note that, for the rest of this manuscript, just to simplify notation, we replace the notation $\widehat{(\tilde{\cdot})}$ with $(\hat{\cdot})$ and also denote n_w as a subscript. In other words, we use $\hat{\omega}_{n_w}(y; k_x)$ and $\hat{F}_{n_w}(y; k_x)$ to represent $\hat{\tilde{\omega}}(y; k_x, n_w)$ and $\hat{\tilde{F}}(y; k_x, n_w)$, respectively.

The basis $\Theta_{n_w}(t)$ is chosen such that it is complete and orthonormal, i.e. $\int_0^T \Theta_{m_w}^* \Theta_{n_w}\, \mathrm{d}t = \delta_{n_w m_w}$, where $\delta_{n_w m_w}$ is the Dirac delta function. The basis could, for instance, be the Fourier basis, where $\Theta_{n_w}(t) = \exp \mathrm{i}(2\pi/T)n_w t$, or as will be considered here, the wavelet basis discussed in § 3.2. In terms of these transforms, the linearised equations in (5.1) become

$$\sum_{n_w=1}^{N_w} \hat{\omega}_{n_w}(y; k_x)\left(\frac{\mathrm{d}\Theta_{n_w}(t)}{\mathrm{d}t}\right) + A\sum_{n_w=1}^{N_w} \hat{\omega}_{n_w}(y; k_x)\Theta_{n_w}(t)$$

$$= \sum_{n_w=1}^{N_w} \hat{F}_{n_w}(y; k_x)\Theta_{n_w}(t). \tag{5.4}$$

Here, N_w is the number of wavelet coefficients obtained from the wavelet transform (determined by the type of wavelet chosen and the number of time instances N_t chosen for the time window). The bases vectors $\Theta_{n_w}(t)$ are not guaranteed to be continuous or differentiable. For instance, the discrete Daubechies 1 wavelet that we use (see § 3.2) is discontinuous and not differentiable. To consider the formulation in terms of the most general bases, including discontinuous ones, we re-write (5.4) in terms of the integrals of the bases $\Theta_{n_w}(t)$, therefore giving us

$$
\sum_{n_w=1}^{N_w} \hat{\omega}_{n_w}(y; k_x)\Theta_{n_w}(t) + A \sum_{n_w=1}^{N_w} \hat{\omega}_{n_w}(y; k_x) \left(\int_0^t \Theta_{n_w}(t')\,dt' \right)
$$
$$
= \sum_{n_w=1}^{N_w} \hat{F}_{n_w}(y; k_x) \left(\int_0^t \Theta_{n_w}(t')\,dt' \right). \tag{5.5}
$$

Since the bases are complete, the integral of a particular basis vector can be written as a linear superposition of all basis vectors, i.e. $\int_0^t \Theta_{n_w}(t')\,dt' = \sum_{m_w=1}^{N_w} c_{n_w m_w}\Theta_{m_w}(t)$, where $c_{n_w m_w}$ are scalar coefficients. This gives

$$
\sum_{n_w=1}^{N_w} \hat{\omega}_{n_w}(y; k_x)\Theta_{n_w}(t) + A \sum_{n_w=1}^{N_w} \hat{\omega}_{n_w}(y; k_x) \left(\sum_{m_w=1}^{N_w} c_{n_w m_w}\Theta_{m_w}(t) \right)
$$
$$
= \sum_{n_w=1}^{N_w} \hat{F}_{n_w}(y; k_x) \left(\sum_{m_w=1}^{N_w} c_{n_w m_w}\Theta_{m_w}(t) \right). \tag{5.6}
$$

Using the orthogonality of the basis vectors, the equation is now rewritten as

$$
\hat{\omega}_{n_w}(y; k_x) + A \sum_{m_w=1}^{N_w} c_{n_w m_w}\hat{\omega}_{m_w}(y; k_x) = \sum_{m_w=1}^{N_w} c_{n_w m_w}\hat{F}_{m_w}(y; k_x). \tag{5.7}
$$

If we were dealing with the Fourier-based equations $c_{n_w m_w} = in_w\delta_{n_w m_w}$. The summations in (5.7) thereby drop off, giving independent equations for each n_w. This is not true for the case of all bases, such as a wavelet bases, where the response at one particular wavelet Θ_{n_w} cannot be isolated from the responses at the other wavelets. In matrix form, this equation will therefore become

$$
\begin{bmatrix} \hat{\omega}_1(y; k_x) \\ \hat{\omega}_2(y; k_x) \\ \hat{\omega}_3(y; k_x) \\ \vdots \end{bmatrix} + \underbrace{\begin{bmatrix} A & 0 & 0 & \dots \\ 0 & A & 0 & \dots \\ 0 & 0 & A & \dots \\ \vdots & \vdots & \vdots & \end{bmatrix} \begin{bmatrix} c_{11}I & c_{12}I & c_{13}I & \dots \\ c_{21}I & c_{22}I & c_{23}I & \dots \\ c_{31}I & c_{32}I & c_{33}I & \dots \\ \vdots & \vdots & \vdots & \end{bmatrix}}_{\bar{A}(y,n_w;k_x)} \begin{bmatrix} \hat{\omega}_1(y; k_x) \\ \hat{\omega}_2(y; k_x) \\ \hat{\omega}_3(y; k_x) \\ \vdots \end{bmatrix}
$$
$$
= \underbrace{\begin{bmatrix} c_{11}I & c_{12}I & c_{13}I & \dots \\ c_{21}I & c_{22}I & c_{23}I & \dots \\ c_{31}I & c_{32}I & c_{33}I & \dots \\ \vdots & \vdots & \vdots & \end{bmatrix}}_{\bar{B}(y,n_w;k_x)} \begin{bmatrix} \hat{F}_1(y; k_x) \\ \hat{F}_2(y; k_x) \\ \hat{F}_3(y; k_x) \\ \vdots \end{bmatrix}. \tag{5.8}
$$

We are considering the discretised equations with N_y number of grid points in the y-direction and N_w wavelets. The matrix A in (5.8) is therefore of size $N_y \times N_y$ and I represents an identity matrix of the same size. The projection coefficients $c_{n_w m_w}$ are scalars. The matrices $\bar{A}(y, n_w; k_x)$ and $\bar{B}(y, n_w; k_x)$ are therefore of sizes $(N_w N_y) \times (N_w N_y)$, and the vectors $\hat{\omega} = [\hat{\omega}_1, \hat{\omega}_2, \dots \hat{\omega}_{N_w}]$ and $\hat{F} = [\hat{F}_1, \hat{F}_2, \dots \hat{F}_{N_w}]$ are each of size $N_y N_w$. Using these definitions, we can write the wavelet-based linearised equation as

$$\hat{\omega}(y, n_w; k_x) + \bar{A}(y, n_w; k_x)\hat{\omega}(y, n_w; k_x) = \bar{B}(y, n_w; k_x)\hat{F}(y, n_w; k_x). \qquad (5.9)$$

To obtain the state-vector $\hat{q}(y, n_w; k_x) = (\hat{u}(y, n_w; k_x), \hat{v}(y, n_w; k_x))$, we introduce an output matrix $\bar{C}$ such that

$$\hat{q}(y, n_w; k_x) = \bar{C}(y, n_w; k_x)\hat{\omega}(y, n_w; k_x). \qquad (5.10)$$

The matrix $\bar{C}$ can also be used to 'mask' the resolvent. For instance, in the upcoming sections, we will compute the responses at specific values of n_w. By selectively including and excluding rows of the matrix $\bar{C}$, we can mask the response such that we obtain responses exclusively at a particular n_w as in § 5.2, or to obtain responses at specific sets of n_w as in § 5.3. It should be noted that, similar to this, the matrix $\bar{B}$ can be used to mask the forcing to the resolvent operator. However, in the present study, we do not mask the forcing. This is because, while we are interested in responses at specific values of n_w that we can separately trace back to the quiet region or the burst events, we do not have a physical argument for restricting the forcing similarly. In the wavelet resolvent, the response at a particular n_w can be forced by all other n_w.

From this point, the procedure to obtain the resolvent operator follows McKeon & Sharma (2010). Rearranging (5.9) gives us

$$\hat{q}(y, n_w; k_x) = \underbrace{\bar{C}[W^{1/2}(I + \bar{A})^{-1} W^{-1/2}]\bar{B}}_{\bar{H}(y, n_w; k_x)} \hat{F}(y, n_w; k_x). \qquad (5.11)$$

Here $\bar{H}(y, n_w; k_x)$ represents the resolvent operator. If a non-uniform grid is used to discretise y, the weight matrix W will contain the weights corresponding to the grid. In this study, we employ a Fourier grid with $N = 51$ grid points, resulting in $W = I$. As for the WPOD (see § 3.2), here the Daubechies 1 wavelets serve as the basis vectors Θ_{n_w}, with a time window of $T = 200$ and a time step of $dt = 1$. A similar wavelet-based operator as that obtained in (5.11) has recently also been used in Ballouz *et al.* (2023*a*,*b*).

5.2. *The WRA response and forcing modes*

Singular value decomposition is used to analyse the resolvent operator, $\bar{H}(y, n_w; k_x)$

$$\bar{H}(y, n_w; k_x) = \sum_{i=1}^{N_y N_w} \boldsymbol{\psi}_i(y, n_w)\sigma_i\phi_i(y, n_w). \qquad (5.12)$$

The singular values are arranged in increasing order such that $\sigma_i \geq \sigma_{i+1}$. The left singular vectors $\boldsymbol{\psi}_i(y, n_w)$ represent the resolvent response modes and the right singular vectors $\phi_i(y, n_w)$ represent the resolvent forcing modes. Essentially, the forcing $\phi_i(y, n_w)$, when put through the resolvent operator, yields a response $\boldsymbol{\psi}_i(y, n_w)$ amplified by σ_i. Both $\boldsymbol{\psi}_i(y, n_w)$ and $\phi_i(y, n_w)$ are functions of y and the wavelets n_w. The most amplified response is $\boldsymbol{\psi}_1(y, n_w)$ corresponding to σ_1, and the corresponding most sensitive forcing direction is $\phi_1(y, n_w)$.
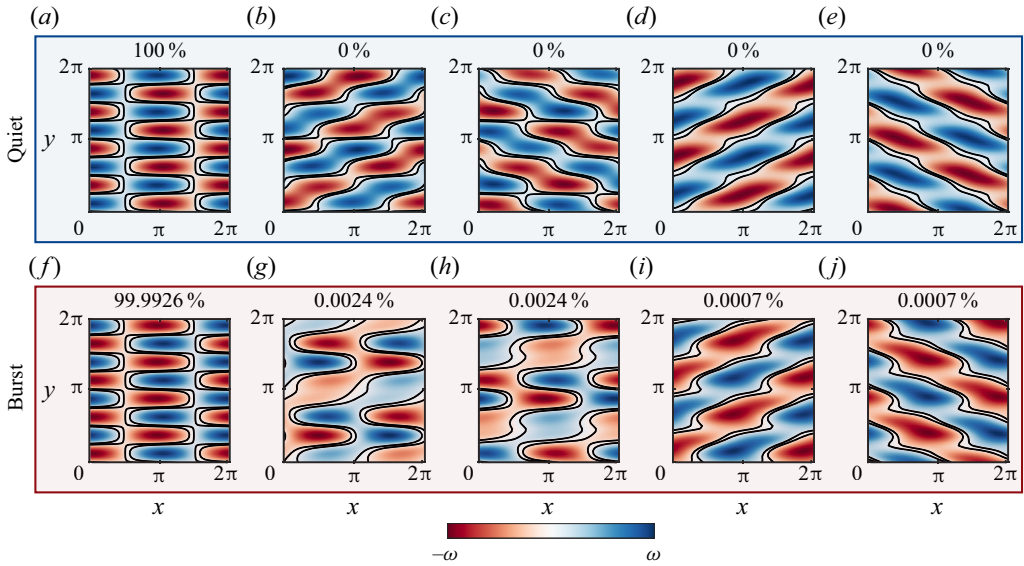
Figure 11. First five resolvent response modes (*a–e*) at $n_w = 2$ that contribute to the quiet region, and (*f–j*) at $n_w = 22$ that contribute to the burst region, are shown. The titles show the fraction of energy (at that n_w) captured by the respective mode, computed as $\sigma_i^2 / \sum_j \sigma_j^2$ (rounded off to eight decimal places for *a–e*).

First, let us consider resolvent response modes at specific values of n_w. To obtain these modes, we can selectively mask specific rows of the output matrix $\bar{C}$ (see (5.10)). For the resolvent, we need to choose a wavenumber in the *x*-direction k_x. The dominant modes in this flow have $k_x = 1$ (see figure 7). Therefore, in figure 11, we show resolvent modes at $k_x = 1$. (The shearing motions in figure 7 can be obtained as $k_x \approx 0$ modes, which are not shown here for the sake of brevity.) Figure 11 shows the resolvent response modes for two values of n_w: (i) $n_w = 2$ that corresponds to the quiet region and (ii) $n_w = 22$ that corresponds to the burst event. The percentages in the title of the figure represent the fraction of energy (at that n_w) captured by the respective mode $\boldsymbol{\psi}_i(y, n_w)$ computed as $\sigma_i^2 / \sum_j \sigma_j^2$.

Consider the modes from the quiet region in the first row of figure 11. The first resolvent mode captures almost the full energy at this n_w (the percentage is rounded off to eight decimal places). The mode corresponds to the unstable eigenfunction of the linearised Navier–Stokes equations (see Appendix A) (Chandler & Kerswell 2013). Crucially, when compared with the first row of figure 6, the first resolvent mode resembles the first WPOD mode. In §4.4, we found that this first WPOD mode dominates the dynamics of the quiet region in DNS. Therefore, for the quiet region, we can conclude that the model is able to predict the dominant structure. Additionally, the model also recognises the significance of this structure, as indicated by the mode capturing almost all the energy at this n_w.

Now consider the modes for the burst event in the second row of figure 11. The first resolvent mode for this n_w is the same as for the quiet region, representing the unstable eigenfunction and capturing the majority of the energy at this n_w. A similar trend was apparent when considering the WPOD modes in figure 6, where we found that the same modes as in the quiet region were also dominant for the burst event, and captured 60 % of the energy of the burst events. In the case of the resolvent modes, however, the quiet region mode captures almost the full energy. Examining the structure of the suboptimal resolvent

1003 A5-24

modes, inclined and fragmented versions of the unstable eigenfunction are apparent, reminiscent of the WPOD modes. For instance, compare figure 7(j) with 11(g). Therefore, for the burst events, the suboptimal resolvent modes do capture the relevant structures. However, the model is not able to identify the significance of these suboptimal modes, as suggested by the percentage of energy captured by them.

5.3. *Reconstructing DNS data using WRA modes*

Our purpose in introducing the resolvent here is to find the forcing structures, i.e. the structures in the nonlinear terms, that produces the quiet region and burst events. Studies have used the Fourier-based resolvent operators to find the underling forcing structures that are important in a flow (e.g. Towne *et al.* 2015; Karban *et al.* 2022). The right and left singular vectors of the resolvent, ϕ_i and ψ_i, form complete bases. Consequently, any response $\hat{q}$, and any forcing $\hat{F}$, that is obtained from data (here from DNS) can be expressed in terms of these basis vectors as

$$\left.\begin{aligned} \hat{F} &= \sum_{i=1}^{N_y N_w} \chi_i \phi_i, \quad \chi_i = \sum_{n_w=1}^{N_w} \int_0^{L_y} \hat{F}_{n_w}(y; k_x)(\phi_i)_{n_w}(y)\, \mathrm{d}y \\ \hat{q} &= \sum_{i=1}^{N_y N_w} \chi_i \sigma_i \psi_i, \quad \chi_i \sigma_i = \sum_{n_w=1}^{N_w} \int_0^{L_y} \hat{q}_{n_w}(y; k_x)(\psi_i)_{n_w}(y)\, \mathrm{d}y, \end{aligned}\right\} \tag{5.13}$$

where $(\phi_i)_{n_w}(y)$ and $(\psi_i)_{n_w}(y)$ are just representing the components of $\phi_i(y, n_w)$ and $\psi_i(y, n_w)$ at a particular n_w. Therefore, given DNS data $\tilde{q}(y, t; k_x)$, we first obtain the wavelet coefficients $\hat{q}_{n_w}(y; k_x)$ through a wavelet transform, and thereafter compute $\chi_i \sigma_i$ by projecting the wavelet coefficients onto the resolvent response modes $\psi_i(y, n_w)$. A reduced-order description of the flow can then be obtained by reconstructing the data using a truncated basis

$$\hat{q}_{approx} = \sum_{i=1}^{N_1} \chi_i \sigma_i \psi_i, \tag{5.14}$$

where N_1 is the number of modes that are retained in the truncated data. The approximate data q_{approx} are then obtained from an inverse wavelet transform in time and an inverse Fourier transform in the x-direction.

From the obtained product $\chi_i \sigma_i$, we then extract χ_i. The N_1 is chosen such that we eliminate modes which contribute less than 0.1 % energy to any particular k_x (i.e. the eliminated modes have $\chi_i \chi_i^* \sigma_i^2$ less than 0.1 % of the energy at that k_x). This χ_i is then used to compute the forcing $\hat{F}_{approx} = \sum_{i=1}^{N_1} \chi_i \phi_i$. The obtained forcing $\hat{F}_{approx}$ when put through the resolvent operator will give a response $\hat{q}_{approx}$. In other words, we can find the component of the full forcing $\hat{F}$ from DNS (i.e. the nonlinear term) that is specifically responsible for amplifying the response $\hat{q}_{approx}$. The forcing F_{approx} (in time) can then be obtained from an inverse wavelet transform in time and an inverse Fourier transform in the x-direction. (It should be noted that, unlike in the case of the Fourier resolvent, the forcing obtained from the wavelet resolvent, $\hat{F}_{approx}$, does not represent a particular spatial mode shape. Instead, $\hat{F}_{approx}$ represents mode shapes at different wavelets n_w. This is because, unlike the Fourier resolvent, for the wavelet resolvent, response at a particular n_w can be forced by multiple separate wavelets simultaneously.)
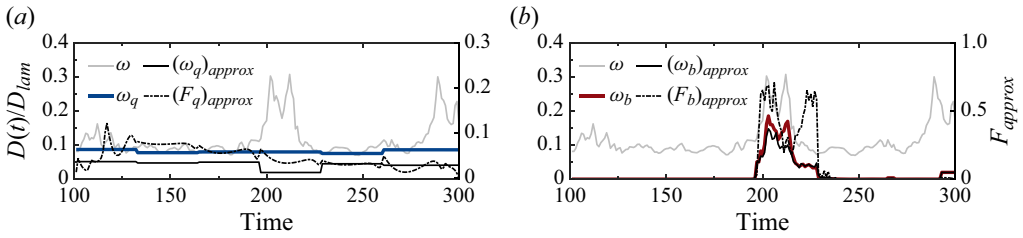
Figure 12. Values of $D(t)/D_{lam}$ computed from the full vorticity data for $k_x = 0, 1, 2, 3$ (grey line) are shown alongside the wavelet-based decomposition of (*a*) the quiet region in blue and (*b*) the burst event in red. The decomposed data are compared with their respective resolvent-based reconstructions (solid black lines). The forcing F_{approx} that generates these responses are also shown (dashed black lines). (The *y*-axis labels on the right in both (*a*) and (*b*) correspond to the forcing.)

To obtain F_{approx} specifically for the quiet region, we obtain resolvent modes for the set of wavelets $\boldsymbol{n}_w^q$ corresponding to the quiet region. The matrix $\bar{C}$ can be used to mask the resolvent so as to obtain a response solely for this particular set of wavelets. The wavelet coefficients obtained from DNS for $\boldsymbol{n}_w^q$ are then projected onto the obtained resolvent modes. Thereafter, following the procedure above, we can obtain the forcing for the quiet region. Similarly, we can also obtain the forcing for the burst region. An illustration of this procedure is shown in figure 12, where figures 12(*a*) and 12(*b*) show the vorticity ω from DNS decomposed into the quiet (blue) and the burst (red) regions, respectively. The corresponding resolvent-based reconstructions ω_{approx} (black solid lines) are also shown, where $(\omega_q)_{approx}$ and $(\omega_b)_{approx}$ represent the reconstructions of the quiet region and the burst events, respectively. Additionally, the forcing F_{approx} that generate these responses are shown (black dashed lines) in these figures. Using WRA, we have therefore constructed forcing $(F_q)_{approx}$ and $(F_b)_{approx}$ that separately generate the quiet region and the burst events, respectively.

5.4. *Coherent structures of the forcing*

Our aim is to identify the coherent structures in the forcing that generates the quiet region and the burst events. In order to find these coherent structures, we first start by using the resolvent to reconstruct the flow field as illustrated in figure 12, and thereby obtain the corresponding forcing. This reconstruction is performed for M different realisations of the quiet region and the burst events (here $M = 50$). Consequently, we obtain M realisations of resolvent-based vorticity reconstructions $(\omega_{approx,1}(x, y, t), \omega_{approx,2}(x, y, t), \ldots, \omega_{approx,M}(x, y, t))$ and the corresponding forcing $(F_{approx,1}(x, y, t), F_{approx,2}(x, y, t), \ldots, F_{approx,M}(x, y, t))$. It is important to note that, for the reconstructions done here, $k_x = (0, 1, 2, 3)$ wavenumbers in the *x*-direction are utilised. Subsequently, to extract the coherent structures, we perform a POD on the M realisations of the forcing. This involves constructing a data matrix P

$$P = [F_{approx,1}(x, y, t_1), F_{approx,1}(x, y, t_2), \ldots, F_{approx,1}(x, y, T),$$
$$F_{approx,2}(x, y, t_1), F_{approx,2}(x, y, t_2), \ldots, F_{approx,2}(x, y, T), \ldots]. \quad (5.15)$$

A SVD of the data matrix P gives us the POD modes. We obtain such POD modes for the quiet region and the burst events.

The top row of figure 13 shows the first few forcing POD modes obtained for the quiet region. The titles of these figures show the percentage of energy that is captured
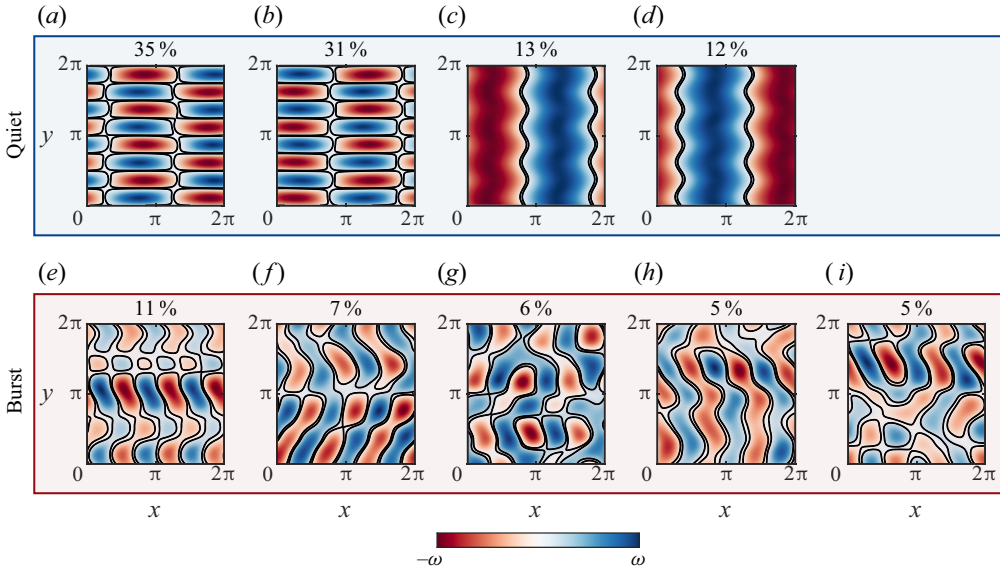
Figure 13. The first few POD modes obtained from the forcing corresponding to the resolvent reconstruction of (a–d) the quiet region and (e–i) the burst events. The titles of these plots show the percentage energy captured by the mode computed as $100 \times \mathcal{E}_i^q / \sum_{j=0}^M \mathcal{E}_j^q$ for the quiet region, and similarly for the burst events.

by the mode. Notably, the first two modes capture a majority of the energy, and the modes resemble the unstable eigenfunction itself. This again suggests that the dominant amplification mechanism is a normal-mode mechanism, where the forcing and response modes can be expected to be structurally similar. Interestingly, modes 3 and 4 resemble the dominant resolvent forcing to the unstable eigenfunction (see Appendix A), which suggests that there is a second route through which the unstable eigenfunction can be amplified. We can also obtain the forcing POD modes for the burst events, and the first five of these modes are shown in the bottom row of figure 13. Notably, inclined structures dominate the forcing to the burst events.

5.5. *Obtaining WRA-based predictions of burst events*

Now that we have identified the coherent structures in the forcing that generate the quiet regions and the burst events, we will track them in a time series obtained from the flow. More specifically, our interest is in analysing how the contributions of these structures to the nonlinear terms of the flow evolve with time. We have two sets of forcing coherent structures: (i) let F_q represent the modes corresponding to the quiet region, with each mode $\phi_i^q(x, y)$ having POD energy $\mathcal{E}_i^q$, and (ii) F_b the modes for the burst event, with each mode $\phi_i^b(x, y)$ having POD energy $\mathcal{E}_i^b$. Both F_q and F_b contain $M \times N_t$ modes, where M is the number of resolvent reconstructions used (here $M = 50$) and N_t is the number of time snapshots of DNS data in each realisation (here, $N_t = 200$). To simplify computation, here, we ignore modes that cumulatively contribute less than 1 % energy (i.e. POD modes k with $\sum_{i=k}^M \mathcal{E}_i^q / \sum_{j=0}^M \mathcal{E}_j^q < 0.01$). At each time t, we aim to assess the presence of the structures in F_q and F_b in the nonlinear terms $F(x, y, t)$ obtained from the flow.

For this purpose, we follow the methodology laid out in § 4.4, with $q(x, y, t)$ now taken to be the nonlinear terms $F(x, y, t)$ obtained from DNS. As explained in § 4.4, we obtain
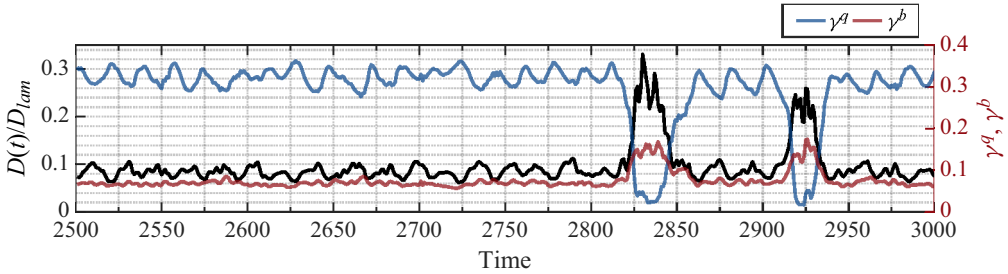
Figure 14. Tracking forcing structures in a time series. The evolution of $\gamma^q(t)$ (blue) and $\gamma^b(t)$ (red) obtained by tracking forcing structures for the quiet region and the burst events, respectively, are shown. Here, $D(t)/D_{lam}$ is also shown (in black).

$\gamma^q(t)$, which is the weighted average of the coherence of the modes in F_q with each point in the time series $F(x, y, t)$. Equivalently, we also obtain $\gamma^b(t)$ for the modes in F_b. (As in § 4.4, we are here interested in the trends of $\gamma^q(t)$ and $\gamma^b(t)$, and not the actual values.) Figure 14 shows the profiles of $\gamma^q(t)$ and $\gamma^b(t)$. We see that $\gamma^q(t)$ and $\gamma^b(t)$ follow distinctive trends during a burst event, with $\gamma^q(t)$ (blue line) decreasing and $\gamma^b(t)$ (red line) increasing. The trends of $\gamma^q(t)$ and $\gamma^b(t)$ can therefore be used for predicting the burst event.

Like in § 4.5, here, we define a predictor $\lambda = \gamma^q(t) - \gamma^b(t)$. Figure 15 shows the evolution of this predictor for three different time windows. (As in § 4.5, here, λ is normalised by the minimum and the maximum values obtained within the time window $t = 0$–15 000.) Using the same method as in § 4.5, we again choose a threshold λ_t. The times when $\lambda < \lambda_t$ are identified as predictions of the burst regions, and the red-shaded regions in figure 15 denote these predictions. These prediction times are compared with the green dashed lines, which denote the predictions obtained from the WPOD-based method in § 4.5. First, we note that, by tracking the forcing structures, we are indeed able to obtain predictions of the burst event. These prediction times are improvements over the WPOD method. We also note that false positives are obtained using this method as well (e.g. $t \approx 17\,195$ in figure 15). As in § 4.5, for a more accurate comparison, we compute the average prediction time τ, the percentage of false positives FP% and the percentage of false negatives FN%. For the WRA-based method $\tau = 1.88$, FP% = 25 and FN% = 4 (compared with $\tau = 1.06$, FP% = 20 and FN% = 2 for the WPOD-based method and $\tau = 0.36$, FP% = 13 and FN% = 0 for the energy-based method). Therefore, the WRA-based method gives improved prediction times in comparison with the WPOD-based method, albeit with slight increases in the false positives and false negatives obtained.

6. A discussion of the predictions obtained

6.1. *A comparison of the three prediction methods*

The prediction methods discussed in this manuscript rely on a predictor going below a threshold value. Therefore, the predictions will vary with this choice of the threshold. The thresholds were chosen as 0.95 times the mean of the predictor λ minus the variance, where these statistics were computed specifically for time instances corresponding to the quiet regions (see § 4.5). Figure 16 illustrates how varying this coefficient 0.95 impacts predictions obtained from the energy-based method in grey, WPOD-based method in green and WRA-based method in red. The comparison between the methods is carried out using the three time averaged quantities defined in § 4.5: (i) average prediction time τ
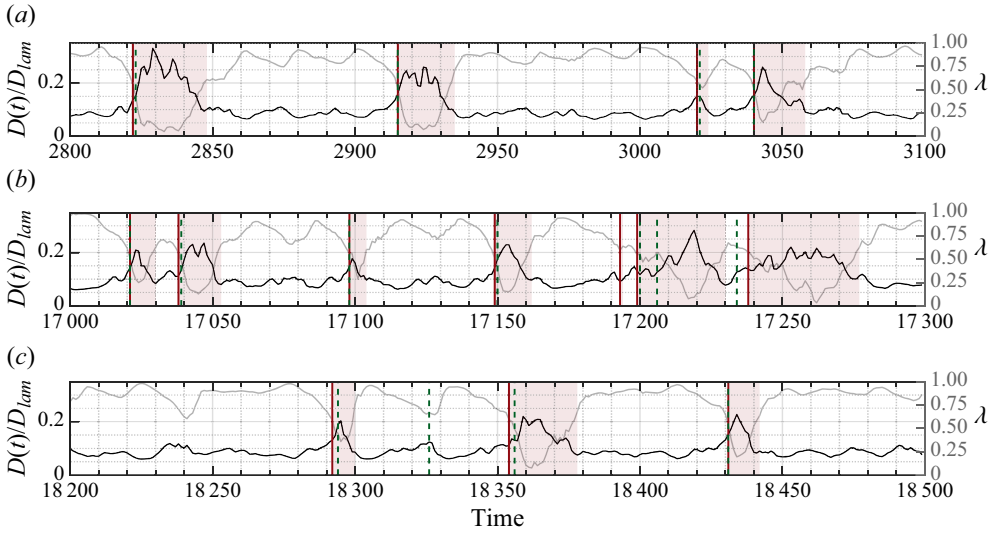
Figure 15. Predictions of the burst events obtained using the WRA-based method for three separate time series from DNS. The red-shaded regions indicate the identified burst regions, where the predictor λ (grey line) goes below the defined threshold value, i.e. $\lambda < 0.95\lambda_t$. The vertical red lines mark the onset of these burst regions, and therefore represent the predictions of the burst event obtained from the WRA-based method. Predicted times are compared with the green dashed vertical lines that indicate the predictions obtained from the WPOD-based method.
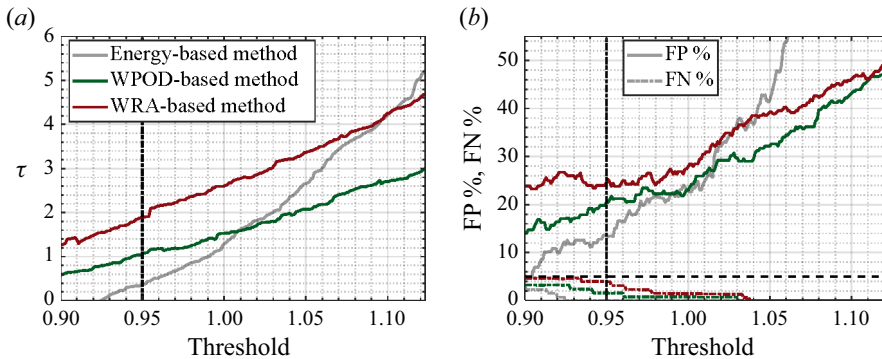

Figure 16. (*a*) The average prediction times τ are shown as a function of the threshold of the predictors for the energy-based method (grey), the WPOD-based method (green) and the WRA-based method (red). (*b*) The percentages of the obtained predictions that are false positives FP% (solid lines) and false negatives FN% (dashed-dot lines) are also shown for the three methods.

in figure 16(*a*), (ii) the percentage of false positives FP% and (iii) the percentage of false negatives FN% in figure 16(*b*).

From figure 16(*a*), we see that, below a threshold value of approximately 1, both the WPOD-based and WRA-based methods give better prediction times than the energy-based method. From figure 16(*b*), we see that this improvement comes at the cost of a slight increase in the number of false positives. Moving back to figure 16(*a*), we see that, above this threshold of approximately 1, the energy-based method starts performing better than the WPOD-based method, but still worse than the WRA-based method. For very high values of the threshold, the energy-based method seems to perform better than both the

wavelet-based methods. However, from figure 16(*b*) we note that this improvement in the performance of the energy-based method comes with a jump in the number of false positives obtained. For the very high thresholds, more than 50 % of the predictions given by the energy-based method are false, i.e. one in two predictions are false. We can therefore conclude that both the wavelet-based methods give a more robust prediction performance when compared with the energy-based method. Additionally, from figure 16(*a*), we see that the WRA-based method always outperforms the WPOD-based method. However, this does come with the cost of a slight increase in the false positives. Finally, considering the false negatives obtained, all three methods give a small number of false negatives. Both the wavelet-based techniques have difficulty in identifying short-lived burst events that exist for 1–2 time units. These events contribute to the false negatives obtained.

(Appendix B shows how this prediction performance changes for a different choice of wavelets, Daubechies 2 instead of the Daubechies 1 used here.)

6.2. *Outlook*

So far, we have looked at two wavelet-based methods to predict intermittent events in a flow: (i) tracking the coherent structures obtained from WPOD and (ii) tracking the forcing structures that generate these coherent structures through the resolvent operator. We illustrated these methods using the 2-D Kolmogorov flow, which is governed by the unstable eigenfunction of the linearised Navier–Stokes equations. The quiet region of this flow is dominated by this unstable eigenfunction, and the burst events seem to happen because of a disruption of this structure. In other words, there is a single eigenfunction of the linearised Navier–Stokes equations that seems to govern the flow. The energy amplification mechanism in this flow therefore is likely a normal-mode amplification mechanism. In this scenario, the resolvent analysis should not actually be expected to give a significant time delay between the forcing and the response.

Contrary to this, we could analyse a flow where the energy amplification occurs due to non-normal mechanisms, such as for instance the streak generation in channel flows. In this case, the forcing will have a time delay from the response. This is due to the transient growth mechanisms that cause energy amplification in non-normal flows (e.g. Trefethen *et al.* 1993; Schmid 2007). In this case, the WRA-based method will likely provide better prediction times in comparison with the WPOD-based method. Comparing these methods for non-normal flows is therefore an important future direction of work.

Applying these methods in practice in experiments would first involve finding the dominant energetic structures or forcing structures. For instance, a calibration experiment with good enough resolution to capture these structures or an large eddy simulation (LES) simulation that captures the relevant dynamics can aid in this purpose. The obtained structures can then be tracked in an experiment at a lower resolution. How sparse these measurements can be, and what spatial regions of the flow the measurements need to be concentrated in, are important questions to be addressed in future work. These factors will also closely depend on the flow considered. For instance, for the flow considered here, although 256 wavenumbers are present in the x-direction, only 7 ($k_x = [-3, -2, -1, 0, 1, 2, 3]$) are required for the POD-based prediction.

7. Conclusions

In this study, we used wavelet-based methods to understand, and therefore predict, high-energy intermittent bursting events in the 2-D Kolmogorov flow at Reynolds number $Re = 40$ forced by a sinusoidal body forcing with wavenumber $n = 4$. In this regime, for

a majority of the time, the flow remains quiet with minor oscillations in energy. This quiet region is occasionally interrupted by intermittent high-energy burst events. The focus was on finding distinctive flow patterns for the quiet regions and the burst events, and thereafter track these structures to obtain predictions of oncoming burst events.

Due to the time-localised nature of the burst events, Fourier-based methods proved inefficient at capturing them (figure 2). Consequently, we used wavelet-based methods (figure 5). Two wavelet-based techniques were employed: (i) WPOD to distinguish the dominant flow patterns of the quiet region and burst events (figure 7), and (ii) WRA to identify forcing structures that generate the quiet region and burst events (figure 13). Subsequently, coherence-based methods were used to track these structures in an evolving time series obtained from the flow. This approach yielded two effective strategies to predict oncoming burst events: (i) the WPOD-based method involved tracking the flow patterns obtained from WPOD (figure 10) and (ii) the WRA-based method involved tracking the forcing patterns obtained from WRA (figure 15). These predictions were then compared with those obtained from the more straightforward energy-based method, which focused on tracking the energy of the flow.

The WPOD analysis revealed three dominant flow patterns (figure 7): (i) the unstable eigenfunction of the linearised Navier–Stokes equations that dominates the quiet region, (ii) shearing structures, also present in the quiet region, and (iii) fragmented or distorted versions of the unstable eigenfunction, crucial during burst events. Tracking these modes revealed that the shearing motions move out of phase with the flow due to the unstable eigenfunction. Moreover, the presence of the unstable eigenfunction decreases during the burst events, while the presence of the fragmented versions of the unstable eigenfunction increases. Based on these observations, we hypothesise that, in the 2-D Kolmogorov flow, shearing motions distort the flow due to the unstable eigenfunction, leading intermittently to burst events. Identifying regions where the flow due to the fragmented or distorted eigenfunctions dominates over the flow due to the eigenfunction itself allowed us to develop the WPOD-based method for predicting oncoming burst events.

Thereafter, using resolvent analysis, we identified the forcing structures that generate the unstable eigenfunction, dominant in the quiet region, as well as inclined forcing structures, dominant during the burst events. Identifying instances when the burst event forcing structures dominate over the quiet region structures led to the development of the WRA-based method of predicting oncoming burst events. Notably, both the WPOD-based and the WRA-based methods were able to predict oncoming burst events and, on average, demonstrated improved prediction times over the energy-based method. However, false positives, where a burst event is predicted while none occurs in the flow, were observed for both methods, with the WRA-based method more prone than the WPOD-based method (figure 16). On the other hand, the WRA-based method gives improved prediction times over the WPOD-based method (figure 16), thereby suggesting that tracking forcing structures might be a more efficient prediction strategy.

The initial expectation was that the WRA-based method would greatly outperform the WPOD-based method. However, for the 2-D Kolmogorov flow, while the WRA-based method does yield improved predictions, the extent of these improvements is not as substantial as initially expected. To understand the underlying reason for this, we can look at the linear mechanisms active in the flow. The dynamics of the 2-D Kolmogorov flow is predominantly governed by the unstable eigenvector of the linearised Navier–Stokes equations. Consequently, the energy amplification mechanism that dominates this flow is likely a normal-mode mechanism. As a result, the appearance of the coherent structures in the flow, and the forcing that generates them, may occur without significant time delay.
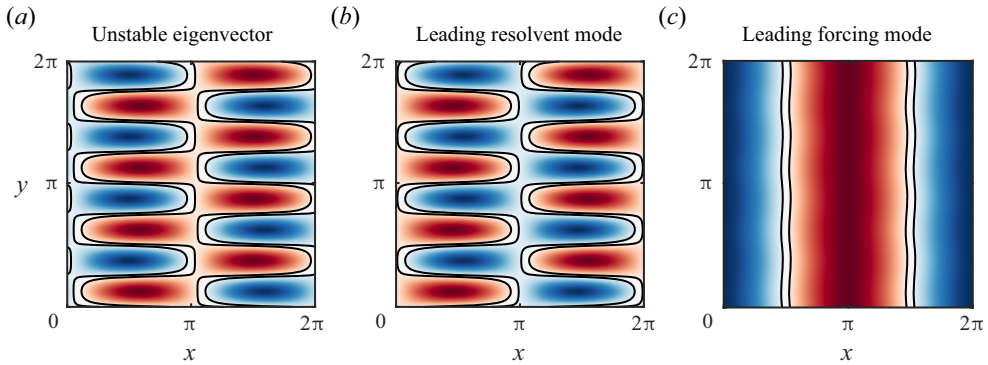
Figure 17. (*a*) The unstable eigenvector of the linearised Navier–Stokes equations is shown for $k_x = 1$. Also shown are the Fourier-based (*b*) resolvent response mode and (*c*) the corresponding forcing mode for a temporal frequency of $\Omega = 0$.

In order to evaluate the prediction methods, there is therefore a requirement to compare the methods in flows where non-normal mechanisms are active. A natural progression to this work, therefore, is to evaluate burst events in wall-bounded flows, that arise from the breakdown of streaks generated by non-normal mechanisms (e.g. Jiménez 2018). We hope to report on findings from this line of research in the near future.

Author ORCIDs.
Ⓓ Anagha Madhusudanan https://orcid.org/0000-0003-3461-3772;
Ⓓ Rich R. Kerswell https://orcid.org/0000-0001-5460-5337.

Appendix A. Unstable eigenvector of the linearised Navier–Stokes equations

Figure 17(*a*) shows the unstable eigenvector of the linearised Navier–Stokes equations for $k_x = 1$ obtained from matrix A in (2.4). The resemblance between the leading WPOD modes obtained in figures 6 and 7 and the unstable eigenvector is evident. Additionally, figure 17(*b*,*c*) presents the Fourier-based resolvent mode for $k_x = 1$ at temporal frequency $\Omega = 0$. The leading resolvent response mode is shown in figure 17(*b*), and this mode is similar to the unstable eigenvector. The corresponding leading forcing mode in figure 17(*c*) therefore represents the forcing that captures the unstable eigenvector. The similarity between this forcing mode, and the suboptimal forcing modes obtained from the WRA method for the quiet region in figure 13 is apparent.

Appendix B. Prediction using Daubechies 2 wavelets

In this section, we reproduce the WPOD-based and the WRA-based prediction performance results, but this time using the Daubechies 2 (DB2) wavelets, instead of the Daubechies 1 (DB1) wavelets used in the rest of the manuscript. Figure 18 shows the
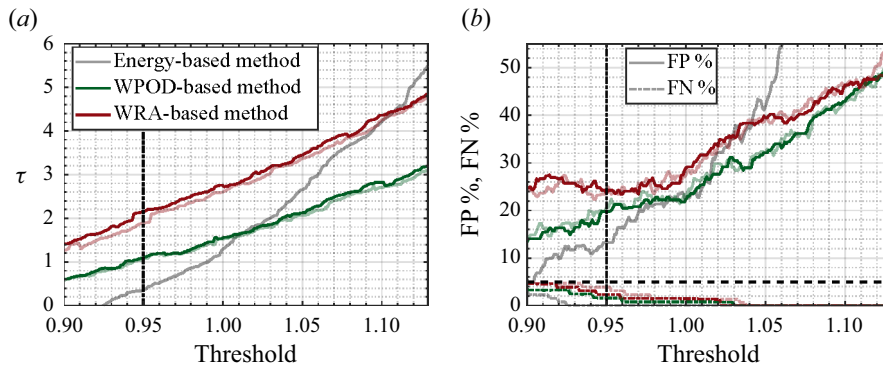
1003 A5-32

Figure 18. The WPOD- and WRA-based predictions obtained using the Daubechies 2 wavelets (dark-coloured lines) are compared with the predictions obtained using the Daubechies 1 wavelets (lines from figure 16 reproduced here as the lighter-coloured lines). (*a*) The average prediction times τ are shown as a function of the threshold of the predictors for the energy-based method (grey), the WPOD-based method (green) and the WRA-based method (red). (*b*) The percentages of the obtained predictions that are false positives FP% (solid lines) and false negatives FN% (dashed-dot lines) are also shown for the three methods.

comparison in figure 16 for predictions using DB2. As in figure 16, two quantities are shown in figure 18. The obtained average prediction times (denoted by τ) in figure 18(*a*), and the percentage of predictions that are false positives FP% and false negatives FN% in figure 18(*b*). The lighter-coloured lines are reproductions of the corresponding lines in figure 16 (i.e. the predictions using DB1) shown here again for comparison. Using DB2 instead of DB1, we obtain marginally improved (earlier) predictions from the WRA-based method. Apart from that, we note that the obtained prediction performances are similar for both DB1 and DB2. This shows that the results are fairly insensitive to the choice of wavelets between DB1 and DB2.

Appendix C. Insensitivity of prediction methods to parameter choices

C.1. *Insensitivity to the exact choice of burst wavelets*

One of the aims of the current section is to show that the prediction results presented here are not sensitive to the selection of wavelets. For a majority of this study, the first three levels of the wavelet transform correspond to the quiet region and 20 % of the most energetic wavelets in the remaining levels represent the burst events. The easiest way to show the insensitivity of the results obtained to this selection, is by performing the same prediction using all the wavelets in the quiet region as well as the burst events. In other words, the wavelets in the first three levels still represent the quiet region, while all the wavelets in levels 4–8 represent the burst events. This, of course, makes the problem computationally a lot more challenging.

The orange curve in figure 19 shows the WPOD-based prediction results when using all wavelets, which can be compared with the original WPOD-based prediction in figure 16, reproduced here as the green line. Two quantities are shown here, the average prediction time τ and the percentage of false positives FP%. We can see that, as per both metrics, the performance of both the methods are similar. Therefore, choosing just the most energetic wavelets for the burst events is the computationally more efficient method to choose. In other words, the method is not sensitive to the choice of wavelets, as long as the most energetic wavelets are still chosen.
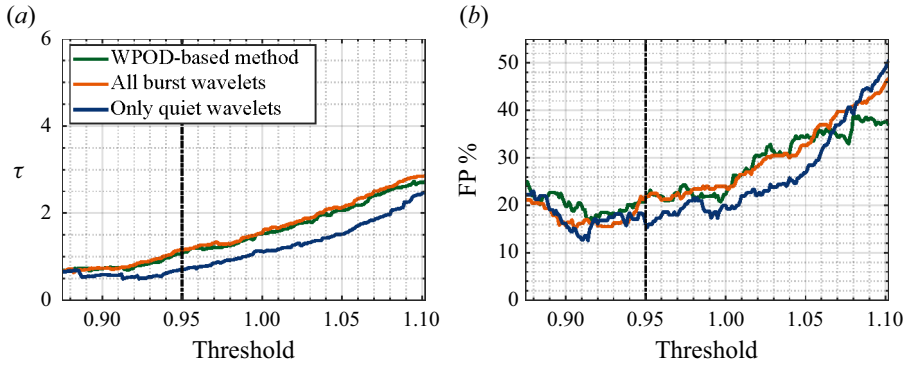
Figure 19. (*a*) The average prediction time τ is shown for two modifications of the WPOD-based method. To obtain the first modified WPOD-based method (orange line), instead of choosing only the most energetic 20 % of the wavelets in the levels corresponding to burst events, all wavelets in those levels are considered. The second modification of the WPOD-based method (blue line) is obtained by defining a predictor using γ^q alone (not including γ^b). The original prediction results from the WPOD-based method, shown in figure 16, are reproduced here for comparison (green line). (*b*) The percentage of the obtained predictions that are false positives is also shown.
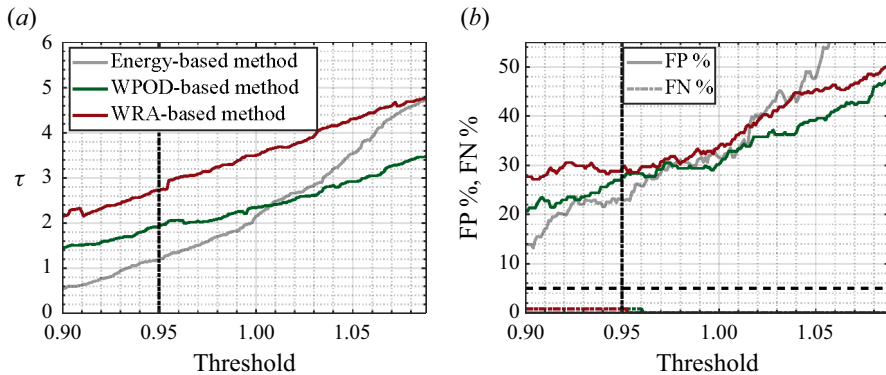

Figure 20. Figure 16 is recreated here with a modified definition of the burst events as times when
$$D(t)/D_{lam} \geq 0.17.$$

C.2. *The WPOD-based method using only the quiet region*

Additionally, here we show how the predictions obtained would vary when considering wavelets in the quiet region alone. We therefore compare predictions obtained using just the quiet region structures with those obtained using the original WPOD-based method. For this purpose, we consider a modified WPOD-based method, where the predictor simply is γ^q (and does not involve γ^b). The dark blue line in figure 19 shows the performance of this predictor, which can be compared with the green line obtained for the original WPOD-based method. We note that the prediction performance of this modified method, based only on the quiet region, is worse than the performance obtained from the original WPOD-based method.

C.3. *Insensitivity to the definition of the burst event*

Finally, the insensitivity of the results to the definition chosen for the burst event is shown here in figure 20. In § 2.2 we choose the definition of a burst event in the 2-D

Kolmogorov flow as times when $D(t)/D_{lam} \geq 0.15$. In figure 16, the comparison of the performances of the three prediction methods was done using this definition of a burst event. Figure 20 shows the same comparison as in figure 16, but with the burst events defined as $D(t)/D_{lam} \geq 0.17$. As expected, although the quantitative values change, the relative trends between the three methods remain the same between figures 16 and 20. Since the conclusions drawn in this manuscript are based on these relative trends between the methods, we can be confident that these conclusions are insensitive to the exact definition of the burst event.

REFERENCES

BABAEE, H. & SAPSIS, T.P. 2016 A minimization principle for the description of modes associated with finite-time instabilities. *Proc. R. Soc. Lond.* A **472** (2186), 20150779.

BALLOUZ, E., DAWSON, S. & BAE, H.J. 2023*a* Transient growth of wavelet-based resolvent modes in the buffer layer of wall-bounded turbulence. arXiv:2312.15465.

BALLOUZ, E., LOPEZ-DORIGA, B., DAWSON, S.T. & BAE, H.J. 2023*b* Wavelet-based resolvent analysis for statistically-stationary and temporally-evolving flows. In *AIAA SCITECH 2023 Forum*, p. 0676. AIAA.

BARTHEL, B. & SAPSIS, T. 2023 Harnessing the instability mechanisms in airfoil flow for the data-driven forecasting of extreme events. arXiv:2303.07056.

BAYINDIR, C. 2016 Early detection of rogue waves by the wavelet transforms? *Phys. Lett.* A **380** (1–2), 156–161.

BLONIGAN, P.J., FARAZMAND, M. & SAPSIS, T.P. 2019 Are extreme dissipation events predictable in turbulent fluid flows? *Phys. Rev. Fluids* **4** (4), 044606.

CHANDLER, G.J. & KERSWELL, R.R. 2013 Invariant recurrent solutions embedded in a turbulent two-dimensional Kolmogorov flow. *J. Fluid Mech.* **722**, 554–595.

DAUBECHIES, I. 1988 Orthonormal bases of compactly supported wavelets. *Commun. Pure Appl. Maths* **41** (7), 909–996.

DOAN, N.A.K., POLIFKE, W. & MAGRI, L. 2021 Short-and long-term predictions of chaotic flows and extreme events: a physics-constrained reservoir computing approach. *Proc. R. Soc.* A **477** (2253), 20210135.

DONZIS, D.A. & SREENIVASAN, K.R. 2010 Short-term forecasts and scaling of intense events in turbulence. *J. Fluid Mech.* **647**, 13–26.

DYSTHE, K., KROGSTAD, H.E. & MÜLLER, P. 2008 Oceanic rogue waves. *Annu. Rev. Fluid Mech.* **40**, 287–310.

FARAZMAND, M. 2016 An adjoint-based approach for finding invariant solutions of Navier–Stokes equations. *J. Fluid Mech.* **795**, 278–312.

FARAZMAND, M. & SAPSIS, T.P. 2016 Dynamical indicators for the prediction of bursting phenomena in high-dimensional systems. *Phys. Rev.* E **94** (3), 032212.

FARAZMAND, M. & SAPSIS, T.P. 2017 A variational approach to probing extreme events in turbulent dynamical systems. *Sci. Adv.* **3** (9), e1701533.

FARAZMAND, M. & SAPSIS, T.P. 2019*a* Closed-loop adaptive control of extreme events in a turbulent flow. *Phys. Rev.* E **100** (3), 033110.

FARAZMAND, M. & SAPSIS, T.P. 2019*b* Extreme events: mechanisms and prediction. *Appl. Mech. Rev.* **71** (5), 050801.

FARGE, M. 1992 Wavelet transforms and their applications to turbulence. *Annu. Rev. Fluid Mech.* **24** (1), 395–458.

FARGE, M., PELLEGRINO, G. & SCHNEIDER, K. 2001 Coherent vortex extraction in 3D turbulent flows using orthogonal wavelets. *Phys. Rev. Lett.* **87** (5), 054501.

FARGE, M. & RABREAU, G. 1988 Transformée en ondelettes pour détecter et analyser les structures cohérentes dans les écoulements turbulents bidimensionnels. *C. R. Acad. Sci. Paris* **307**, 1479–1486.

FARGE, M., SCHNEIDER, K. & DEVYNCK, P. 2006 Extraction of coherent bursts from turbulent edge plasma in magnetic fusion devices using orthogonal wavelets. *Phys. Plasmas* **13** (4), 042304.

FARGE, M., SCHNEIDER, K., PELLEGRINO, G., WRAY, A.A. & ROGALLO, R.S. 2003 Coherent vortex extraction in three-dimensional homogeneous turbulence: comparison between CVS-wavelet and POD-Fourier decompositions. *Phys. Fluids* **15** (10), 2886–2896.

FLORYAN, D. & GRAHAM, M.D. 2021 Discovering multiscale and self-similar structure with data-driven wavelets. *Proc. Natl Acad. Sci. USA* **118** (1), e2021299118.

FOX, A.J., CONSTANTE-AMORES, C.R. & GRAHAM, M.D. 2023 Predicting extreme events in a data-driven model of turbulent shear flow using an atlas of charts. *Phys. Rev. Fluids* **8** (9), 094401.

GUPTA, S., SHANBHOGUE, S., SHIMURA, M., GHONIEM, A. & HEMCHANDRA, S. 2022 Impact of a centerbody on the unsteady flow dynamics of a swirl nozzle: intermittency of precessing vortex core oscillations. *J. Engng Gas Turbines Power* **144** (2), 021014.

GUTH, S. & SAPSIS, T.P. 2019 Machine learning predictors of extreme events occurring in complex dynamical systems. *Entropy* **21** (10), 925.

HWANG, Y. & COSSU, C. 2010 Linear non-normal energy amplification of harmonic and stochastic forcing in the turbulent channel flow. *J. Fluid Mech.* **664**, 51–73.

JIMÉNEZ, J. 2018 Coherent structures in wall-bounded turbulence. *J. Fluid Mech.* **842**, P1.

KARBAN, U., MARTINI, E., CAVALIERI, A.V.G., LESSHAFFT, L. & JORDAN, P. 2022 Self-similar mechanisms in wall turbulence studied using resolvent analysis. *J. Fluid Mech.* **939**, A36.

KRAH, P., ENGELS, T., SCHNEIDER, K. & REISS, J. 2022 Wavelet adaptive proper orthogonal decomposition for large-scale flow data. *Adv. Comput. Math.* **48** (2), 10.

LUMLEY, J.L. 1967 The structure of inhomogeneous turbulent flows. In *Atmospheric Turbulence and Radio Wave Propagation* (ed. A.M. Yaglom & V.I. Tatarski), pp. 166–178. Nauka.

LUMLEY, J.L. 1970 *Stochastic Tools in Turbulence*. Academic Press.

MCKEON, B.J. & SHARMA, A.S. 2010 A critical-layer framework for turbulent pipe flow. *J. Fluid Mech.* **658**, 336–382.

MENEVEAU, C. 1991 Analysis of turbulence in the orthonormal wavelet representation. *J. Fluid Mech.* **232**, 469–520.

MOARREF, R., SHARMA, A.S., TROPP, J.A. & MCKEON, B.J. 2013 Model-based scaling of the streamwise energy density in high-Reynolds number turbulent channels. *J. Fluid Mech.* **734**, 275–316.

MORRA, P., NOGUEIRA, P.A.S., CAVALIERI, A.V.G. & HENNINGSON, D.S. 2021 The colour of forcing statistics in resolvent analyses of turbulent channel flows. *J. Fluid Mech.* **907**, A24.

NEELIN, J.D., BATTISTI, D.S., HIRST, A.C., JIN, F.-F., WAKATA, Y., YAMAGATA, T. & ZEBIAK, S.E. 1998 ENSO theory. *J. Geophys. Res.* **103** (C7), 14261–14290.

PAGE, J., BRENNER, M.P. & KERSWELL, R.R. 2021 Revealing the state space of turbulence using machine learning. *Phys. Rev. Fluids* **6** (3), 034402.

PYRAGAS, V. & PYRAGAS, K. 2020 Using reservoir computer to predict and prevent extreme events. *Phys. Lett.* A **384** (24), 126591.

QI, D. & MAJDA, A.J. 2020 Using machine learning to predict extreme events in complex systems. *Proc. Natl Acad. Sci. USA* **117** (1), 52–59.

RACCA, A. & MAGRI, L. 2022 Data-driven prediction and control of extreme events in a chaotic flow. *Phys. Rev. Fluids* **7** (10), 104402.

REN, J., MAO, X. & FU, S. 2021 Image-based flow decomposition using empirical wavelet transform. *J. Fluid Mech.* **906**, A22.

ROBINSON, S.K. 1991 Coherent motions in the turbulent boundary layer. *Annu. Rev. Fluid Mech.* **23** (1), 601–639.

ROWLEY, C.W. & DAWSON, S.T.M. 2017 Model reduction for flow analysis and control. *Annu. Rev. Fluid Mech* **49**, 387–417.

RUDY, S.H. & SAPSIS, T.P. 2022 Prediction of intermittent fluctuations from surface pressure measurements on a turbulent airfoil. *AIAA J.* **60** (7), 4174–4190.

SAPSIS, T.P. 2021 Statistics of extreme events in fluid flows and waves. *Annu. Rev. Fluid Mech.* **53**, 85–111.

SCHMID, P.J. 2007 Nonmodal stability theory. *Annu. Rev. Fluid Mech.* **39**, 129–162.

SCHMID, P.J. 2022 Dynamic mode decomposition and its variants. *Annu. Rev. Fluid Mech.* **54**, 225–254.

SCHMID, P.J., GARCÍA-GUTIERREZ, A. & JIMÉNEZ, J. 2018 Description and detection of burst events in turbulent flows. *J. Phys.: Conf. Ser.* **1001**, 012015.

SCHMIDT, O.T. & SCHMID, P.J. 2019 A conditional space–time POD formalism for intermittent and rare events: example of acoustic bursts in turbulent jets. *J. Fluid Mech.* **867**, R2.

SCHNEIDER, K. & VASILYEV, O.V. 2010 Wavelet methods in computational fluid dynamics. *Annu. Rev. Fluid Mech.* **42**, 473–503.

SRIRANGARAJAN, S., ALLEN, M., PREIS, A., IQBAL, M., LIM, H.B. & WHITTLE, A.J. 2013 Wavelet-based burst event detection and localization in water distribution systems. *J. Signal Process. Syst.* **72**, 1–16.

TAIRA, K., BRUNTON, S.L., DAWSON, S.T.M., ROWLEY, C.W., COLONIUS, T., MCKEON, B.J., SCHMIDT, O.T., GORDEYEV, S., THEOFILIS, V. & UKEILEY, L.S. 2017 Modal analysis of fluid flows: an overview. *AIAA J.* **55** (12), 4013–4041.

TOWNE, A., COLONIUS, T., JORDAN, P., CAVALIERI, A.V. & BRES, G.A. 2015 Stochastic and nonlinear forcing of wavepackets in a Mach 0.9 jet. In *21st AIAA/CEAS Aeroacoustics Conference. AIAA Paper* 2015-2217.

TOWNE, A., LOZANO-DURÁN, A. & YANG, X. 2020 Resolvent-based estimation of space–time flow statistics. *J. Fluid Mech.* **883**, A17.

TOWNE, A., SCHMIDT, O.T. & COLONIUS, T. 2018 Spectral proper orthogonal decomposition and its relationship to dynamic mode decomposition and resolvent analysis. *J. Fluid Mech.* **847**, 821–867.

TREFETHEN, L.N., TREFETHEN, A.E., REDDY, S. & DRISCOLL, T.A. 1993 Hydrodynamic stability without eigenvalues. *Science* **261**, 578–584.

WAN, Z.Y., VLACHAS, P., KOUMOUTSAKOS, P. & SAPSIS, T. 2018 Data-assisted reduced-order modeling of extreme events in complex dynamical systems. *PLoS ONE* **13** (5), e0197704.

YEUNG, P.K., ZHAI, X.M. & SREENIVASAN, K.R. 2015 Extreme events in computational turbulence. *Proc. Natl Acad. Sci. USA* **112** (41), 12633–12638.